

# Carbon Monoxide Binding to the Iron–Molybdenum Cofactor of Nitrogenase: a Detailed Quantum Mechanics/Molecular Mechanics Investigation

Nico Spiller, Ragnar Bjornsson,\* Serena DeBeer,\* and Frank Neese\*

Cite This: *Inorg. Chem.* 2021, 60, 18031–18047

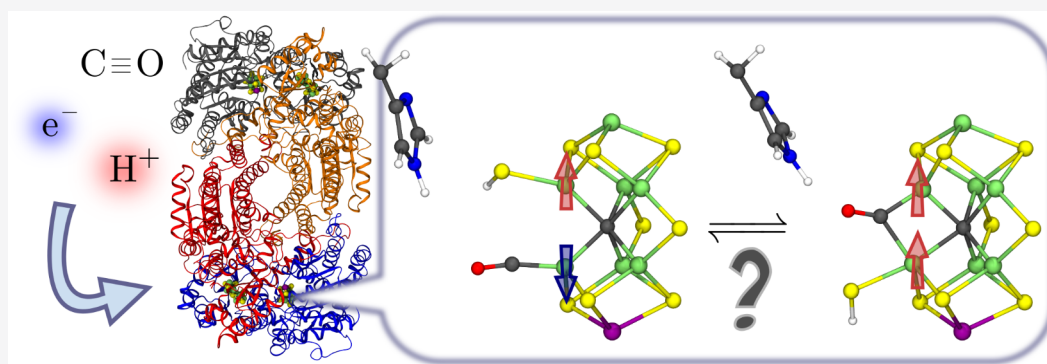
Read Online

ACCESS |

Metrics & More

Article Recommendations

Supporting Information



**ABSTRACT:** Carbon monoxide (CO) is a well-known inhibitor of nitrogenase activity. Under turnover conditions, CO binds to FeMoco, the active site of Mo nitrogenase. Time-resolved IR measurements suggest an initial terminal CO at  $1904\text{ cm}^{-1}$  that converts to a bridging CO at  $1715\text{ cm}^{-1}$ , and an X-ray structure shows that CO can displace one of the bridging belt sulfides of FeMoco. However, the CO-binding redox state(s) of FeMoco ( $E_n$ ) and the role of the protein environment in stabilizing specific CO-bound intermediates remain elusive. In this work, we carry out an in-depth analysis of the CO–FeMoco interaction based on quantum chemical calculations addressing different aspects of the electronic structure. (1) The local electronic structure of the Fe–CO bond is studied through diamagnetically substituted FeMoco. (2) A cluster model of FeMoco within a polarizable continuum illustrates how CO binding may affect the spin-coupling between the metal centers. (3) A QM/MM model incorporates the explicit influence of the amino acid residues surrounding FeMoco in the MoFe protein. The QM/MM model predicts both a terminal and a bridging CO in the  $E_1$  redox state. The scaled calculated CO frequencies ( $1922$  and  $1716\text{ cm}^{-1}$ , respectively) are in good agreement with the experimentally observed IR bands supporting CO binding to the  $E_1$  state. Alternatively, an  $E_2$  state QM/MM model, which has the same atomic structure as the CO-bound X-ray structure, features a semi-bridging CO with a scaled calculated frequency ( $1718\text{ cm}^{-1}$ ) similar to the bridging CO in the  $E_1$  model.

## INTRODUCTION

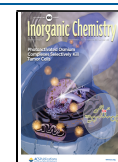
Nitrogenases are a group of enzymes that can reduce chemically inert  $\text{N}_2$  to bioavailable ammonia. The best studied class of nitrogenase is Mo nitrogenase.<sup>1</sup> Here, the proteins required for  $\text{N}_2$  reduction are the Fe protein and the MoFe protein, with the Fe protein functioning as an electron donor to the MoFe protein. Inside the MoFe protein, the electron is transferred *via* the P-cluster, an  $\text{Fe}_8\text{S}_7$  cluster, to the active site, where  $\text{N}_2$  is reduced. The active site is a large iron–sulfur cluster called the iron molybdenum cofactor (FeMoco). It contains seven Fe, a single Mo, and an unusual carbide ( $\text{C}^{4-}$ ) as the central atom.<sup>2,3</sup> The reduction of  $\text{N}_2$  is a complex, little-understood process that requires a total of eight electrons and eight protons being transferred to FeMoco. The individual states in the catalytic cycle are labeled  $E_n$  according to the Lowe–Thorneley cycle,<sup>4</sup> where  $n$  refers to the reduction events

relative to the resting state  $E_0$ . The  $E_4$  state is thought to be the primary redox state that binds  $\text{N}_2$ , and the binding event is generally believed to happen as reductive elimination of  $\text{H}_2$  occurs.<sup>5</sup> The alternative V and Fe nitrogenases contain V or only Fe instead of Mo in their active site,<sup>6</sup> but all three nitrogenases are believed to follow highly similar  $\text{N}_2$  reduction mechanisms.<sup>7</sup>

Several other small molecules can act as substrates or inhibitors to nitrogenase such as acetylene, propargyl alcohol,

Received: August 26, 2021

Published: November 12, 2021



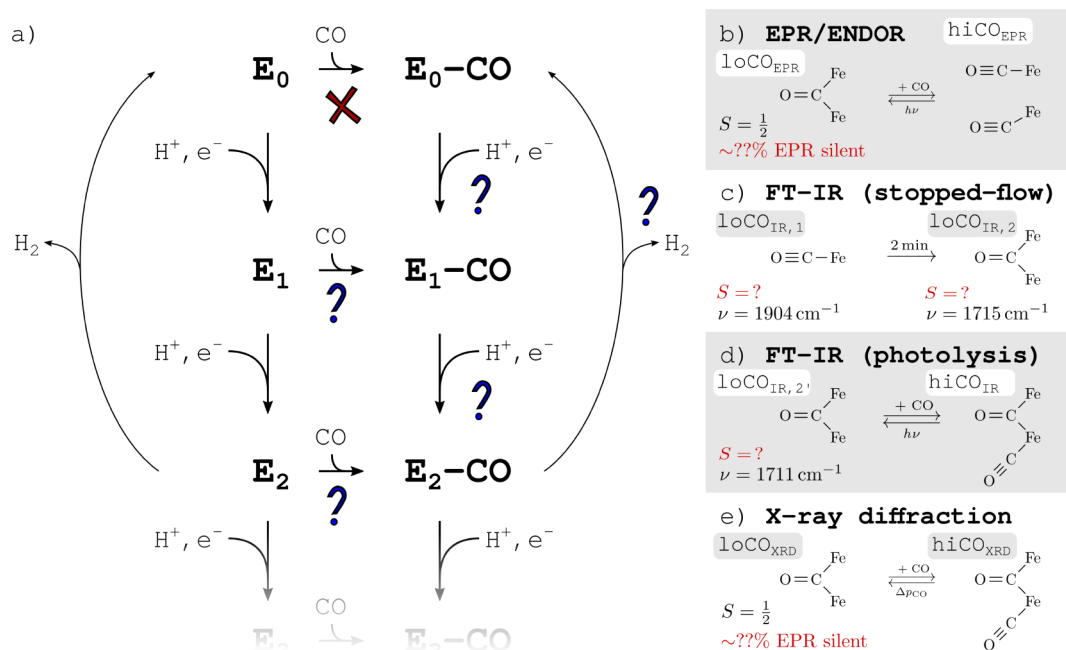


**Figure 1.** (a) Early  $E_n$  redox states in the Lowe–Thorneley cycle for nitrogen reduction by Mo nitrogenase and possible CO inhibition. In the resting state of the wild-type MoFe protein ( $E_0$ ), the active site FeMoco gives rise to an  $S = 3/2$  EPR signal, which is not perturbed in the presence of CO. (b–e) Proposed experimental species with a single CO bound to FeMoco in the MoFe protein: EPR/ENDOR spectroscopy (b), FT-IR spectroscopy (c,d), and X-ray crystallography (e). The single CO species appear under low CO partial pressures and can bind a second CO under high CO partial pressures.

cyanide, or carbon monoxide (CO).<sup>8</sup> CO is isoelectronic to  $N_2$  and has been known for several decades to diminish nitrogenase-dependent plant growth.<sup>9</sup> In the wild-type MoFe protein, CO binds reversibly to the active site and is an inhibitor to  $N_2$  reduction. Furthermore, it is generally accepted that CO binding in the wild-type MoFe protein requires turnover conditions, that is, the supply of electrons and protons to the active site, and is believed to happen during the early states in the Lowe–Thorneley cycle ( $E_1$  or  $E_2$ ), as illustrated in Figure 1a.<sup>10</sup> However, V nitrogenase has been reported to bind CO without turnover conditions in the presence of a reductant.<sup>11,12</sup> Interestingly, V nitrogenase, as well as Fe nitrogenase and Val70 mutants of Mo nitrogenase, have been shown to catalytically reduce CO to hydrocarbons.<sup>13–15</sup>

The experimental techniques that have been employed most often for the study of CO binding to nitrogenase are electron paramagnetic resonance (EPR) and infrared (IR) spectroscopy. With IR spectroscopy, one probes all species irrespective of the  $E_n$  state. EPR spectroscopy, on the other hand, is typically spin state-selective and routinely probes only even-numbered  $E_n$  states. While a number of CO-bound IR and EPR species have been reported (*vide infra*), a parallel study of both techniques, which could establish a correspondence between them and further indicate their respective  $E_n$  state, has not been reported to date. Figure 1b–e gives an overview of the proposed structures based on the experimental observations which are discussed in the following text.

In the resting state  $E_0$ , MoFe-bound FeMoco gives rise to an  $S = 3/2$  EPR signal ( $g = [4.33, 3.77, 2.00]$ ).<sup>16</sup> The charge of FeMoco has been established as  $[MoFe_7S_9C]^{1-}$ ,<sup>17–19</sup> with 41 unpaired electrons being shared among the metal centers (assuming  $Fe^{2+}$ ,  $Fe^{3+}$ , and  $Mo^{3+}$  oxidation states). In the  $E_1$  state, FeMoco has an even number of electrons, but the spin

state—either diamagnetic or integer spin—is currently unknown. It has recently been proposed based on QM/MM calculations that the Fe part of the Mo cubane is reduced in the  $E_1$  state compared to the  $E_0$  state.<sup>20,21</sup> Additionally, multiple computational studies have proposed the belt sulfide S2B or S5A being protonated in the  $E_1$  state.<sup>20,22–25</sup> In the  $E_2$  state, FeMoco exhibits two distinct  $S = 3/2$  EPR signals ( $g = [4.21, 3.76, 1.97]/[4.69, 3.20, 2]$ ).<sup>26–29</sup> Computational models have suggested that hydride formation can occur in this redox state.<sup>22,24,29,30</sup>

The presence of CO does not alter the  $E_0$  EPR signal of the MoFe protein, which suggests no interaction between CO and FeMoco in the wild-type resting state MoFe protein. However, under turnover conditions, the presence of CO generates two characteristic  $S = 1/2$  EPR signals:  $loCO_{EPR}$  and  $hiCO_{EPR}$ , that arise under low and high CO pressures, respectively ( $g = [2.09, 1.97, 1.93]/[2.17, 2.06]$ , labeled lo-CO/hi-CO in the original work).<sup>31</sup>  $^{57}Fe$  electron nuclear double resonance (ENDOR) measurements on the  $loCO_{EPR}$  and  $hiCO_{EPR}$  species confirm that CO binds to FeMoco.<sup>32</sup> The symmetry of the hyperfine coupling tensor extracted from  $^{13}C$ -ENDOR spectra leads to the proposition that the  $loCO_{EPR}$  species harbors a single bridging  $\mu$ -CO ligand and  $hiCO_{EPR}$  two terminal CO ligands (see Figure 1b).<sup>33</sup> It is possible to convert the  $hiCO_{EPR}$  species to  $loCO_{EPR}$  by photolysis, and subsequent annealing restores  $hiCO_{EPR}$  with an estimated activation energy of about 1 kcal/mol, implying that  $loCO_{EPR}$  and  $hiCO_{EPR}$  arise from the same, even-numbered  $E_n$  state.<sup>34</sup> Furthermore, the valence assignment based on  $^{57}Fe$  ENDOR studies suggest that the  $loCO_{EPR}$  and  $hiCO_{EPR}$  species, as well as the resting state, have the same formal metal oxidation states.<sup>35</sup> However, spin quantification for these EPR signals has not been reported for the wild-type MoFe protein but only for the His195→Gln mutant, which gives rise to identical  $loCO_{EPR}$  and  $hiCO_{EPR}$  signals under

comparable conditions. These  $\text{loCO}_{\text{EPR}}$  and  $\text{hiCO}_{\text{EPR}}$  signals have been reported to constitute merely 10 and 26% of the total reaction mixture, respectively, while the resting state  $S = 3/2$  signal amounts to 8%.<sup>36</sup> It has been shown for the His195→Gln mutant that a single CO can be photolysed from a two CO bound species without affecting the EPR spectrum.<sup>37</sup> Further spin quantification of the EPR spectrum showed a large fraction of FeMoco in an EPR-silent state. These observations suggest that CO binding may also occur at the  $E_1$  state.

The binding of CO to FeMoco under turnover conditions was followed by time-resolved stopped-flow FTIR (SF-FT-IR) spectroscopy.<sup>38–40</sup> The electron-flux and CO pressure were comparable to those used in EPR studies (*vide supra*). Under low CO partial pressures, a single transient vibrational band appears at  $1904\text{ cm}^{-1}$  ( $\text{loCO}_{\text{IR},1}$ ), which is fully converted into a band at  $1715\text{ cm}^{-1}$  within 2 min ( $\text{loCO}_{\text{IR},2}$ ). The bands were proposed to correspond to a terminal CO that transforms to a bridging  $\mu$ -CO (see Figure 1c). Under high CO partial pressures, multiple bands were observed between 1700 and  $2000\text{ cm}^{-1}$ . Two of those bands, at  $1906$  and  $1715\text{ cm}^{-1}$ , respectively, closely follow a time course of the  $1904$  and  $1715\text{ cm}^{-1}$  bands at low CO pressures. Therefore, the  $\text{loCO}_{\text{IR},1}$  and  $\text{loCO}_{\text{IR},2}$  species observed under low CO pressures are very likely present under high CO pressures as well. The SF-FT-IR experiment with high CO partial pressures was repeated for Val70→Ile and Val70→Gly mutants.<sup>40</sup> With the more bulky Ile residue, the frequency of the  $\text{loCO}_{\text{IR},1}$  species shifts from  $1906\text{ cm}^{-1}$  (wild-type) to  $1895\text{ cm}^{-1}$  and with the spatially less demanding Gly to  $1911\text{ cm}^{-1}$ . It is of interest to note that CO inhibits the reduction of azide by Mo nitrogenase within less than 400 ms and therefore happens faster than the appearance of the  $\text{loCO}_{\text{IR},1}$  signal.<sup>41</sup>

The multitude of species present under high CO pressures were characterized further by IR-monitored photolysis.<sup>37,42</sup> Particularly, the photolysis of  $\text{hiCO}_{\text{IR}}$  to  $\text{loCO}_{\text{IR},2'}$  (Hi-1 and Lo-1 in the original work) is related to the IR species already discussed (see Figure 1d).  $\text{hiCO}_{\text{IR}}$  exhibits two frequencies that are consistent with a terminal CO and a bridging  $\mu$ -CO. After photolysis to  $\text{loCO}_{\text{IR},2'}$ , a band at  $1711\text{ cm}^{-1}$  indicates a bridging CO, while a second signal corresponds to an unbound CO molecule trapped in some protein pocket. Considering the similar frequencies, the species  $\text{loCO}_{\text{IR},2'}$  most likely corresponds to the SF-FT-IR species  $\text{loCO}_{\text{IR},2}$  ( $1715\text{ cm}^{-1}$ ). Annealing of  $\text{loCO}_{\text{IR},2'}$  leads to the recovery of the  $\text{hiCO}_{\text{IR}}$  bands. The estimated activation energy for this conversion of about 1 kcal/mol is in good agreement with the reversible conversion between the EPR species  $\text{loCO}_{\text{EPR}}$  and  $\text{hiCO}_{\text{EPR}}$ , suggesting that the detached CO is trapped in a similar protein pocket.

Furthermore, CO binding has also been reported for solution-extracted FeMoco following electrochemical reduction.<sup>43–45</sup> Here, the authors observed no interaction of CO with solvated FeMoco in an oxidation state showing an  $S = 3/2$  EPR signal and therefore most likely corresponding to the  $E_0$  state of the MoFe protein. However, after one-electron reduction, a single IR band at  $1835\text{ cm}^{-1}$  is observed under low CO pressures, which is replaced by a band at  $1808\text{ cm}^{-1}$  upon further reduction. Based on the low frequency, the authors interpret both signals as arising from a bridging CO. Also, cyanide has been shown to enable CO binding to the supposedly  $E_0$ -like redox state of solvated FeMoco.<sup>45</sup>

An X-ray diffraction (XRD) structure of the MoFe protein has been solved after putting the system under turnover with low CO partial pressures.<sup>46</sup> In this  $1.5\text{ \AA}$  X-ray structure ( $\text{loCO}_{\text{XRD}}$ ), a  $\mu$ -CO was found to replace the S2B belt sulfide, which bridges Fe2 and Fe6 in the resting state (see Figure 1d). Such a structure is consistent with a bridging CO that has been proposed for  $S = 1/2$  EPR species  $\text{loCO}_{\text{EPR}}$  and the SF-FT-IR species  $\text{loCO}_{\text{IR},2}$ . More recently, a  $1.33\text{ \AA}$  X-ray structure was obtained by exposing the  $\text{loCO}_{\text{XRD}}$  crystals to high CO pressures.<sup>47</sup> The resulting X-ray structure ( $\text{hiCO}_{\text{XRD}}$ ) is actually a superposition of the singly and the doubly CO-bound cofactors. An EPR spectrum shows the presence of  $\text{loCO}_{\text{EPR}}$  for the low-pressure samples and a mixture of  $\text{loCO}_{\text{EPR}}$  and  $\text{hiCO}_{\text{EPR}}$  for the high-pressure samples. Nevertheless, an unambiguous correspondence between the XRD and EPR species cannot be firmly established, as spin quantification of the EPR signals was not reported and hence possible contributions from EPR-silent states are unaccounted for.

Multiple structures of a singly CO-bound FeMoco have been proposed based on density functional theory (DFT) calculations. Rod and Nørskov proposed terminal CO binding to either Fe2, Fe3, or Fe4 based on a FeMoco cluster model and found significantly stronger binding for an  $E_1$ - and an  $E_2$ -type model as compared to  $E_0$ .<sup>48</sup> Dance suggested the possibility that the vibration of terminal CO is coupled to the Fe–H stretching of a hydride bound to the same Fe center.<sup>49</sup> The above-mentioned studies, however, assumed either no central atom or a nitride ( $\text{N}^{3-}$ ), but not a carbide ( $\text{C}^{4-}$ ), as determined later experimentally.<sup>2,3</sup> Varley and Nørskov proposed a mechanism for CO reduction to methane by an isolated FeMoco model featuring the central carbide.<sup>50</sup> According to a cluster model by Scott *et al.*, the experimental SF-FT-IR species  $\text{hiCO}_{\text{IR}}$  arises from an  $E_2$ -type cofactor with one terminal CO and one terminal formyl (HCO) species.<sup>51</sup> With the exception of the QM/MM model used in the quantum refinement of the X-ray structure  $\text{loCO}_{\text{XRD}}$ ,<sup>52</sup> none of the computational studies of the CO–FeMoco interaction to date have explicitly included the protein environment. However, the importance of the protein environment has been demonstrated by a number of experimental studies which report distinct CO binding characteristics for multiple MoFe protein mutants.<sup>37,40,42,51,53</sup>

While  $\text{N}_2$  reduction is believed to follow highly similar mechanisms for all three nitrogenases (Mo, V, and Fe),<sup>7</sup> they exhibit significant differences for CO as a substrate/inhibitor, as explained above.<sup>11–15,54</sup> In wild-type Mo nitrogenase, CO merely inhibits the catalytic activity, which allows for a cleaner interpretation of the available experimental data. Therefore, in this study, we will focus on the CO-bound intermediates in the wild-type MoFe protein. Within the present study, we would like to address the following questions: (1) What oxidation and protonation states of the cofactor are required for CO binding? (2) What is the initial binding site of CO? (3) How does the protein environment affect the binding of CO? To this end, we examine different  $E_n$  states, different binding sites (Fe2 and Fe6), and different models for the environment (dielectric continuum *vs* explicit QM/MM). The first part of this study focuses on the local electronic structure of the Fe–CO bond. The second part deals with the complete cofactor in the resting state  $E_0$ . A parallel investigation of a cluster model and a QM/MM model shows the explicit effects of the protein environment on CO binding. The third part focuses on the

more reduced  $E_1$  and  $E_2$  models. Finally, the results are discussed in the context of the experimentally observed species in Figure 1b–e.

## ■ COMPUTATIONAL DETAILS

The QM/MM model was constructed based on the  $E_0$  model of the MoFe protein described previously.<sup>18</sup> This model has been shown to accurately reproduce the cofactor geometry of the corresponding 1.0 Å high-resolution X-ray structure. The QM region in this work includes FeMoco, all residues that directly bind FeMoco, as well as proximal charged residues, and residues surrounding Fe2 and Fe6: FeMoco, homocitrate, His442, Cys275, His195, Gln191, Val70, Arg96, Arg359, Tyr229, and Ser278. The protein backbone of the residues was not included, except for the Ser residue, because the amide forms a hydrogen bond with the sulfide of Cys275. The QM region is shown in Figure S1. For the  $E_1$  QM/MM model, an additional proton was added to the S2B belt sulfide following a recently combined QM/MM and extended X-ray absorption fine structure (EXAFS) study that suggested protonation of a belt sulfide (S2B or possibly SSA) to occur in the  $E_1$  redox state.<sup>20</sup> The CO-bound structures reported herein were optimized by relaxing the active region (about 1000 atoms). CO was initially placed at about 1.8 Å from either Fe6 or Fe2. CO and  $\text{SH}^-$  in the  $E_1$  models were found to coordinate both in a terminal and in a bridging mode depending on the tested broken-symmetry (BS) determinant (*vide infra*). Therefore, all combinations of (i) a terminal CO and a terminal  $\text{SH}^-$ , (ii) a terminal CO and a bridging  $\mu\text{-SH}^-$ , and (iii) a bridging  $\mu\text{-CO}$  and a terminal  $\text{SH}^-$  were tested in order to find all relevant local minima. In the QM/MM  $\Delta\text{His195}$  model, the atoms of the His195 side chain were simply deleted from the QM region, and the His195 residue is therefore completely absent in this model. The QM/MM  $\Delta\text{His195}$  model is not further optimized after the deletion, and the energies reported refer to the energy of the QM region in the field of the MM charges.

The QM regions were calculated with the ORCA program suite, version 4.2.<sup>55–57</sup> The hybrid density functional TPSSh was used, which includes 10% Hartree–Fock (HF) exchange.<sup>58,59</sup> A low HF exchange in the hybrid density functional has been shown to yield accurate geometries for FeS clusters.<sup>60–62</sup> Furthermore, calculations with TPSSh have successfully reproduced the X-ray structure of the resting state MoFe protein<sup>18,63</sup> as well as key features in the X-ray absorption spectroscopy (XAS) spectra of FeS clusters, such as the relationship between the pre-edge area in S K-edge XAS spectra and the Fe oxidation state in  $\text{Fe}_2\text{S}_2$  dimers.<sup>64</sup>

Dispersion forces were approximated with the atom-pairwise post-DFT correction by Grimme including Becke–Johnson damping (D3BJ in ORCA).<sup>65,66</sup> Scalar relativistic effects were modeled by the zeroth order regular approximation (ZORA).<sup>67,68</sup> All electron basis sets of the Karlsruhe-type recontracted for ZORA were used (ZORA-def2-XVP).<sup>69,70</sup> Unless noted otherwise, the basis set of triple- $\zeta$  quality ( $X = \text{TZ}$ ) was used for all metals, the sulfurs, the central carbide, the CO molecule, the added proton in the  $E_1$  models, and the homocitrate, while double- $\zeta$  ( $X = \text{S}$ ) was used for the remaining atoms. Coulomb and HF exchange integrals were approximated with resolution of identity Coulomb approximation and chain-of-spheres exchange (RIJCOSX)<sup>71,72</sup> employing the auxiliary basis set SARC/J.<sup>70</sup>

The CHARMM36 force field was used to describe the non-QM protein environment, which was modified to include non-

bonding parameters for the FeS clusters as previously described.<sup>18,73</sup> The coupling between the QM and MM Hamiltonians (using electrostatic embedding) was calculated using a custom version of ChemShell, based on version 3.7.<sup>74,75</sup> A link to the ChemShell setup including the modified parameter files is made available in the Supporting Information.

The nomenclature of the BS determinants in this paper follows the classification introduced by Noodleman *et al.* with the added three-digit label indicating the spin-flipped Fe centers.<sup>76</sup> For example, the label BS7-235 indicates that in this BS determinant the centers Fe2, Fe3, and Fe5 carry an excess  $\beta$  spin and that the determinant belongs to the Noodleman class 7. The members of a class are related by the symmetry operations of the  $C_{3v}$  point group. A BS determinant was generated with the FlipSpin procedure implemented in ORCA. The high-spin multiplicity for the resting state, substrate-free cofactor was 36, assuming all local high-spin metal centers and the formal oxidation states  $[\text{Fe}_3^{\text{II}}\text{Fe}_4^{\text{III}}\text{Mo}^{\text{III}}\text{S}_9\text{C}]^{1-}$  (number of unpaired electrons:  $3 \times 4 (\text{Fe}^{2+}) + 4 \times 5 (\text{Fe}^{3+}) + 3(\text{Mo}^{3+}) = 35$ ).<sup>17</sup> The high-spin multiplicity was reduced by 2 for each  $E_n \rightarrow E_{n+1}$  reduction event because the reduction is expected to be Fe-centered (*i.e.*  $\text{Fe}^{3+} \rightarrow \text{Fe}^{2+}$ ),<sup>20</sup> and it is further reduced by 2 when CO was bound because CO has been shown to induce local spin-pairing (*vide infra*). The calculated BS determinants include the three members of the BS7 class (BS7-235, BS7-247, and BS7-346), because they have been shown to constitute the lowest-energy models for the resting state FeMoco.<sup>18,77–79</sup> Also, the BS10-147 determinant has been calculated because it constitutes a low-energy model for the QM/MM models of the  $E_4$  state,<sup>63,80</sup> as well as BS10-135, which is the mirror image of BS10-147 with respect to Fe6/Fe2.

The cluster models were created from the substrate-free  $E_0$  QM/MM model (BS7-235 with  $M_s = 3/2$ ).<sup>18</sup> The cluster models consist only of the cofactor, the homocitrate, the His residue bound to Mo, and the Cys residue bound to Fe1. The computational protocol was analogous to the QM/MM models with three exceptions: (1) the triple- $\zeta$  basis was used for all atoms. (2) Instead of the MM embedding, the surroundings were described with the conductor-like polarizable continuum model (C-PCM) with a dielectric constant of  $\epsilon = 4$ .<sup>81,82</sup> (3) During the geometry optimizations, the position of the homocitrate, His, and Cys residue were constrained; only the cofactor  $[\text{Fe}_7\text{MoS}_9\text{C}]$  and CO were allowed to relax.

CO binding energies were calculated as  $\Delta E = E_{\text{AB}} - (E_{\text{A}} + E_{\text{B}})$ , where  $E_{\text{AB}}$ ,  $E_{\text{A}}$ , and  $E_{\text{B}}$  are the total electronic energies of the CO-bound system, the substrate-free system, and unbound CO, respectively. The electronic energies correspond reasonably well to the enthalpy of the cofactor. The calculated binding enthalpy  $\Delta H$  differs by less than 1 kcal/mol from the binding electronic energy (tested for the  $E_1$  cluster model with CO bound to Fe6 considering all vibrations of CO and FeMoco:  $\Delta E = -15.0$  kcal/mol and  $\Delta H = -14.1$  kcal/mol). Entropic effects are discussed separately in the text.

The total electronic energies of all tested substrate-free models are shown in Figure S3, and those of all tested CO-bound models are given in Figure S4 (cluster model) and Figure S5 (QM/MM model). The metal–metal distances for the lowest-energy models are given in Table S2, and the geometries of the respective QM regions are attached as xyz files.

The CO vibrational frequency was calculated by diagonalizing the partial Hessian matrix of only the CO coordinates and the binding Fe center(s). It was found that the frequency remains virtually the same when including more atoms (see Table S3). All reported frequencies were scaled so that the as-calculated frequency of CO in vacuum ( $2181\text{ cm}^{-1}$ ) matches the experimental IR frequency of CO gas ( $2143\text{ cm}^{-1}$ ).<sup>83</sup> Therefore, all calculated frequencies were multiplied by 0.9826. Both as-calculated and scaled frequencies are listed in Table S3.

In diamagnetic substitution, most magnetic metal centers are replaced by diamagnetic ions with a similar ionic radius, which has proven useful for studying the complex electronic structure of FeS clusters.<sup>84–86</sup> According to the localized orbital analysis of the complete cofactors, the Fe centers in FeMoco have an intermediate oxidation state in between  $\text{Fe}^{3+}$  and  $\text{Fe}^{2+}$  (a result of delocalized electrons being shared between Fe centers<sup>18</sup>) and neither  $\text{Ga}^{3+}$  nor  $\text{Zn}^{2+}$  are a suitable diamagnetic equivalent for Fe in FeMoco. To emulate an intermediate oxidation state, the atomic charge of Ga was lowered to  $Z = 30.5$ , as this resulted in sulfide atomic charges closer to the unsubstituted cofactors compared to normal Ga atoms ( $Z = 31$ ) or normal Zn atoms ( $Z = 30$ ). Therefore, diamagnetically substituted cofactors were constructed by replacing Mo with In and Fe with modified Ga ( $Z = 30.5$ ). For the  $\text{CO}-[\text{FeGa}_6\text{InS}_9\text{C}]^{2+,1+,0}$  and  $\text{CO}-[\text{Fe}_2\text{Ga}_5\text{InS}_9\text{C}]^{1+}$  models, the lowest-energy  $E_0$  cluster model with CO bound to Fe6 was used and all metal centers but Fe6 (or Fe6/Fe2) were substituted. Only the positions of CO were relaxed to account for CO activation and in order to calculate the CO frequency. Analogous calculations for CO bound to Fe2 led to qualitatively equivalent results. For  $\mu\text{-CO}-[\text{Fe}_2\text{Ga}_5\text{InHS}_9\text{C}]^{2+}$ , the structure of the converged  $E_1$  QM/MM model with CO bridging Fe6 and Fe2 was used (see Figure 5). The CO coordinates were not optimized further after the diamagnetic substitution because the bridging binding motif was only stable for the  $E_1$  QM/MM model. Therefore, no CO frequency was calculated for  $\mu\text{-CO}-[\text{Fe}_2\text{Ga}_5\text{InHS}_9\text{C}]$ .

Localized orbitals were generated with the Foster–Boys algorithm as implemented in ORCA.<sup>87</sup> The complete set of metal/CO-based localized orbitals is given for the QM/MM models in Figure S6 (substrate-free), Figure S7 (CO-bound in  $E_0$ ), and Figure S8 (CO-bound in  $E_1$ ). All orbital populations, atomic charges, and spin populations are reported within the Hirshfeld partitioning scheme,<sup>88</sup> as implemented in the wave function analyzer program Multiwfn,<sup>89</sup> version 3.7, using precalculated neutral atom densities to construct the density of the promolecule (default in Multiwfn). The Hirshfeld-I scheme was also tested, which is an extension to the original scheme, where the atomic volumes and hence the charges are iteratively refined<sup>90</sup> but was found unstable as the charge of the central carbide diverges. The atomic spin populations and charges of the lowest-energy models are listed in Tables S5 and S6, respectively. Molecules and orbitals were rendered with the VMD visualization program, version 1.9.3.<sup>91</sup> Orbitals are plotted with isosurfaces at  $\pm 0.05$  (solid) and  $\pm 0.025$  (transparent). Atom colors are Mo: purple, Fe: green, Ga/In: black, S: yellow, C: gray, O: red, N: blue, H: white.

## RESULTS AND DISCUSSION

**Electronic Structure of FeCO Fragments.** The electronic structure of a transition-metal complex depends on its ligand field, which is determined by the coordination geometry

and the nature of the ligands.<sup>92</sup> CO induces a large ligand field splitting and typically leads to spin-pairing at the metal site.<sup>93</sup>  $\pi$  back bonding from suitable metal orbitals to the antibonding  $\pi^*$  orbitals on CO weakens and therefore activates the C–O bond. On the other hand, the tetrahedral Fe sites in biological FeS clusters usually maintain a local high spin in the weak ligand field of the  $\text{S}^{2-}$  ligands. It is not *a priori* evident how the interaction between CO and the Fe centers in FeMoco relates to these two extremes, and it is therefore instructive to discuss the influence of a CO ligand on the local electronic structure of an Fe center in the chemical environment of FeMoco. To this end, all metal centers except the center(s) of interest were replaced by a diamagnetic metal ion in a simple cluster model of the cofactor:  $\text{Ga}^{3+}$  replaces Fe and  $\text{In}^{3+}$  replaces Mo, both of which have a  $d^{10}$  configuration. These ions have similar ionic radii as Fe and Mo, respectively, in the chemical environment of FeMoco and therefore exert a similar electrostatic influence, but they do not engage in the more complicated spin–spin interaction. Thus, diamagnetic substitution generates Fe–CO fragments that are more relevant for a CO–FeMoco adduct than, for example, model complexes with multiple CO ligands coordinated to the same Fe center. This partial substitution of magnetic centers with diamagnetic ions has been shown to aid the understanding of the complex electronic structure in FeS clusters by separating local and cooperative effects.<sup>84–86</sup>

**Terminal CO Binding.** The simplest and the most common CO binding mode is a terminal coordination of a metal center *via* the carbon atom. To study this binding mode in FeMoco, we created an  $[\text{FeGa}_6\text{InS}_9\text{C}]$  complex by substituting all Fe except the Fe6 center by Ga and furthermore Mo by In. These diamagnetic substituents are shown with black atoms in Figure 2a. Similarly, binding CO to Fe2 in the Fe-only cubane was found to give qualitatively equivalent results.

Prior to CO binding, the single Fe center in  $[\text{FeGa}_6\text{InS}_9\text{C}]^{2+,1+,0}$  is a high-spin center for the three oxidation states  $\text{Fe}^{3+,2+,1+}$ . This is in line with the expectations for an approximately tetrahedral, weak ligand field created by three sulfides and one carbide ligand. Binding CO leads to stable, bound structures with a pentacoordinate Fe center for all three Fe oxidation states ( $\text{CO}-[\text{FeGa}_6\text{InS}_9\text{C}]^{2+,1+,0}$ ). In all three cases, an intermediate spin state is the most stable, as can be seen in the corresponding orbital occupation schemes in Figure 2a. The  $z^2$  orbital is exclusively unoccupied. Going from oxidized to more reduced Fe, the orbitals are filled in the order  $xz$ ,  $yz$ , and  $x^2-y^2$ . This behavior meets the expectations for a CO ligand, which is both a  $\sigma$ -donor and a  $\pi$ -acceptor and therefore destabilizes Fe orbitals along the Fe–CO bond ( $z^2$ ) but stabilizes the Fe orbitals that overlap with the CO  $\pi^*$  orbitals ( $xz$  and  $yz$ ).

The Fe–CO distance in  $\text{CO}-[\text{FeGa}_6\text{InS}_9\text{C}]^{2+,1+,0}$  decreases from 1.85 to 1.76 to 1.71 Å, respectively (see Table 1). At the same time, the C–O bond length is 0.017, 0.032, and 0.054 Å longer compared to unbound CO (1.129 Å at the same level of theory). The shorter Fe–CO and the longer C–O bond correlate with the more electron-rich Fe center in  $[\text{FeGa}_6\text{InS}_9\text{C}]$ . Note that the change in the C–O bond length is larger between  $\text{Fe}^{3+}$  and  $\text{Fe}^{2+}$ , but the change in the Fe–CO bond length is larger between  $\text{Fe}^{2+}$  and  $\text{Fe}^{1+}$ . Therefore, the amount of CO activation does not necessarily correlate with the length of the Fe–CO bond.

Similar to the C–O bond length, the calculated CO vibrational frequency in  $\text{CO}-[\text{FeGa}_6\text{InS}_9\text{C}]^{2+,1+,0}$  captures CO activation and decreases from 1978 to 1884 to 1772

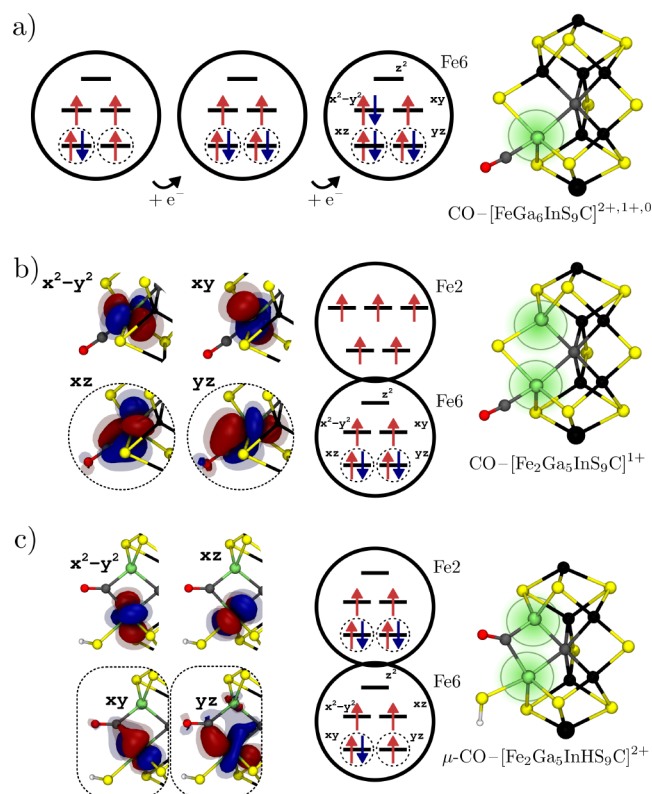


**Figure 2.** Structures of the diamagnetically substituted CO-bound cofactors and the localized orbitals for the indicated charge states: (a) CO bound terminally to the single Fe center in  $[\text{FeGa}_6\text{InS}_9\text{C}]^{2+,1+,0}$ . (b) CO bound terminally to one of two Fe centers in  $[\text{Fe}_2\text{Ga}_5\text{InS}_9\text{C}]^{1+}$ . (c) CO bridging the two Fe centers in  $[\text{Fe}_2\text{Ga}_5\text{InHS}_9\text{C}]^{2+}$  (open  $\text{SH}^-$  bridge). Diamagnetic metal centers are shown in black (Fe/Mo replaced with Ga/In, respectively). Orbitals with significant Fe–CO overlap are highlighted by dashed circles. The orbital labels correspond to a local coordinate system in which the  $z$  axis is oriented along the respective Fe–carbide bond and the  $x$  and the  $y$  axes lie within and perpendicular to the Fe2/Fe6/carbide plane, respectively. For orbitals that are not shown: the Fe2 orbitals (b,c) are mirror images of Fe6. The Fe6 orbitals in (a) are equivalent to the Fe6 orbitals in (b).

$\text{cm}^{-1}$ , respectively. The frequencies for the  $\text{Fe}^{3+}$  and  $\text{Fe}^{2+}$  oxidation states correspond reasonably well to experimentally observed frequencies for terminally bound CO to FeMoco (between 1900 and 1980  $\text{cm}^{-1}$ ).<sup>37–39,42</sup> The calculated CO frequency is lowered by about 100  $\text{cm}^{-1}$  upon the reduction of  $\text{Fe}^{3+ \rightarrow 2+}$  as well as  $\text{Fe}^{2+ \rightarrow 1+}$ . The additional electron in the  $\text{Fe}^{1+}$  oxidation state occupies the  $x^2-y^2$  orbital (no overlap with CO  $\pi^*$  orbitals), but the overlap of the  $xz$  and  $yz$  orbitals with CO increases for  $\text{Fe}^{2+ \rightarrow 1+}$ . Therefore, reducing an Fe center also

activates the CO bond even if the additional electron is not directly involved in the  $\pi$  back bond.

Next, the influence of a neighboring Fe center on the Fe–CO bond is explored by “reactivating” Fe2 in addition to Fe6 while keeping diamagnetic ions for the remaining metal centers ( $\text{CO}-[\text{Fe}_2\text{Ga}_5\text{InS}_9\text{C}]^{1+}$  in Figure 2b). According to BS-DFT models of the resting state FeMoco, both Fe6 and Fe2 have  $\text{Fe}^{2.5+}$  oxidation states due to being part of delocalized mixed-valence pairs in their respective cubanes.<sup>18</sup> CO binding to Fe6 leads to charge localization, and the oxidation states of Fe6 and Fe2 become  $\text{Fe}^{2+}$  and  $\text{Fe}^{3+}$ , respectively. The orbital occupation pattern on Fe6 is analogous to  $\text{Fe}^{2+}$  in  $\text{CO}-[\text{FeGa}_6\text{InS}_9\text{C}]^{1+}$ , with an unoccupied  $z^2$  orbital and doubly occupied  $xz$  and  $yz$  orbitals resulting in the same local intermediate spin. The neighboring Fe2 has a local highspin.

Compared to  $\text{CO}-[\text{FeGa}_6\text{InS}_9\text{C}]^{1+}$ , the Fe–CO bond length in is 0.012 Å longer, the C–O bond length is 0.004 Å shorter, and the CO frequency is 24  $\text{cm}^{-1}$  higher (see Table 1). Therefore, the strength of the Fe–CO bond and the amount of CO activation is slightly lower in ( $\text{Fe}^{2+}\text{Fe}^{3+}$  fragment) compared to  $\text{CO}-[\text{FeGa}_6\text{InS}_9\text{C}]^{1+}$  ( $\text{Fe}^{2+}$  fragment). A closer inspection of the orbitals in  $\text{CO}-[\text{Fe}_2\text{Ga}_5\text{InS}_9\text{C}]^{1+}$  reveals that some Fe6-based localized orbitals also show small contributions from Fe2. Because the neighboring Fe center allows for electron delocalization toward Fe2, the Fe–CO bond is weakened compared to a single  $\text{Fe}^{2+}$  magnetic center.

In biological  $[\text{Fe}_2\text{S}_2]^{2+}$  clusters, the two local high-spin ferric centers typically exhibit a strong antiferromagnetic coupling to a diamagnetic ground state.<sup>94</sup> Thinking of larger FeS clusters as consisting of smaller fragments, it has been proposed for FeMoco that those spin alignments, that is, BS determinants, are the most stable that contain the maximum number of antiferromagnetically coupled Fe pairs.<sup>76,95</sup> These are the determinants belonging to the BS7 class, namely, BS7-235, BS7-247, and BS7-346, and they constitute the lowest-energy determinants in the resting state MoFe QM/MM model.<sup>18,77–79</sup> The coupling strength between two magnetic centers can be quantified by the coupling constant  $J$ . Using the spin Hamiltonian  $\hat{H}_S = -2J\hat{S}_A\hat{S}_B$ , a negative value indicates antiferromagnetic coupling. The coupling constant for an Fe pair can be easily extracted from diamagnetically substituted FeMoco with BS-DFT by keeping only two magnetic centers ( $[\text{Fe}_2\text{Ga}_5\text{InS}_9\text{C}]^{1+}$ ). Focusing on the Fe6/Fe2 pair, the calculated coupling constant prior to CO binding is  $-117 \text{ cm}^{-1}$  in  $[\text{Fe}_2\text{Ga}_5\text{InS}_9\text{C}]^{1+}$ , and the two Fe centers are therefore antiferromagnetically coupled. However, after CO binding, the coupling constant for the Fe6/Fe2 pair becomes  $+34 \text{ cm}^{-1}$ . The change in the coupling constant with CO binding is clearly a result of the spin-pairing on Fe6 (see Figure 2b), and the local intermediate spin Fe center has a reduced preference

**Table 1.** Fe–CO Bond Parameters in the Diamagnetically Substituted Cofactors That Relate to CO Activation<sup>a</sup>

	binding mode	$S_{\text{pop}}^b$		$\nu_{\text{CO}}^c$ [ $\text{cm}^{-1}$ ]	$d_{\text{C-O}}$ [Å]	$d_{\text{Fe-CO}}$ [Å]
		Fe6	Fe2			
$\text{CO}-[\text{FeGa}_6\text{InS}_9\text{C}]^{2+,1+,0}$	CO– $\text{Fe}^{3+}$	2.50		1978	1.146	1.850
	CO– $\text{Fe}^{2+}$	1.84		1884	1.161	1.756
	CO– $\text{Fe}^{1+}$	1.04		1772	1.183	1.710
$\text{CO}-[\text{Fe}_2\text{Ga}_5\text{InS}_9\text{C}]^{1+}$	CO– $\text{Fe}^{2+}\text{Fe}^{3+}$	2.05	3.58	1908	1.157	1.768
$\mu\text{-CO}-[\text{Fe}_2\text{Ga}_5\text{InHS}_9\text{C}]^{2+}$	$\mu\text{-CO}-\text{Fe}^{2+}\text{Fe}^{3+}$	2.29	2.50		1.193	1.837/1.960

<sup>a</sup>Corresponding structures and orbital occupation schemes are shown in Figure 2. <sup>b</sup>Spin populations are based on the Hirshfeld partitioning scheme. <sup>c</sup>Scaled vibrational frequencies. See Table S3 for unscaled frequencies.

for antiferromagnetic alignment with its neighbors. This suggests that the binding of a  $\pi$ -accepting ligand (CO or even  $N_2$ ) may affect the stability of BS determinants in FeMoco.

**Bridging CO Binding.** CO bridging Fe6 and Fe2 has been observed in the X-ray structure  $loCO_{XRD}$  and has also been proposed as the binding mode in the EPR species  $loCO_{EPR}$  and the IR species  $loCO_{IR,2}$ . We will explain the origins of this bridging CO structure later in this study when discussing the  $E_1$  QM/MM model but use the structure already at this point to explore the bridging CO binding motif through diamagnetic substitution. In this structure, CO has replaced the S2B belt sulfide as the bridging ligand between Fe6 and Fe2, while the sulfide is still bound to Fe6 as a terminal  $SH^-$  ligand. The C–O bond in the bridging CO structure is 0.032 Å longer than the terminal CO in  $CO-[Fe_2Ga_3InS_9C]^{1+}$  (Table 1). At the same time, the two Fe–CO bonds are about 0.1–0.2 Å longer than the single bond in  $CO-[Fe_2Ga_3InS_9C]^{1+}$ .

The corresponding diamagnetically substituted model  $\mu-CO-[Fe_2Ga_3InHS_9C]^{2+}$  is shown in Figure 2c. The orbital occupation scheme indicates the oxidation states  $Fe^{3+}$  and  $Fe^{2+}$  for Fe6 and Fe2, respectively, which is the opposite electron distribution compared to the terminal  $CO-[Fe_2Ga_3InS_9C]^{1+}$ . Since CO forms an asymmetric bridge, the reason for the more oxidized Fe6 appears to be the  $SH^-$  ligand coordinated to Fe6. In contrast to the substrate-free FeMoco, both Fe6 and Fe2 exhibit a local intermediate spin state because the  $z^2$  orbital, which is oriented along the respective Fe–carbide bond, is unoccupied in both centers. This definition of the local coordinate systems on Fe6 and Fe2 also implies that the Fe orbitals which overlap with the  $\pi^*$  orbitals of the bridging CO are the  $xy$  and the  $yz$  orbitals (in contrast to the  $xz$  and  $yz$  orbitals for terminal CO). Furthermore, one has to distinguish between the in-plane and out-of-plane contributions to the  $\pi$  back bonding. The  $xy$  orbital (out-of-plane) is doubly occupied on both Fe centers, but the  $yz$  orbital (in-plane) is doubly occupied only on Fe2. Therefore, the out-of-plane  $\pi$  back bonding *via* the  $xy$  orbitals appears to be energetically favored for a bridging CO in FeMoco. The longer C–O bond length compared to terminal CO, despite the significantly longer Fe–CO bond lengths, is consistent with two Fe centers contributing to the  $\pi$  back bonding instead of one.

The calculated coupling constant for the Fe6/Fe2 pair in  $\mu-CO-[Fe_2Ga_3InHS_9C]^{2+}$  is  $+47\text{ cm}^{-1}$ . The ferromagnetic coupling of Fe6 and Fe2 bridged by CO is even stronger compared to the terminally bound CO in  $CO-[Fe_2Ga_3InS_9C]^{1+}$  ( $+34\text{ cm}^{-1}$ ). The reason could be either the additional spin-pairing or the replacement of the bridging  $\mu-S^{2-}$ , which favors antiferromagnetic coupling in  $Fe_2S_2$  dimers.<sup>85</sup>

**Lessons Learned from Diamagnetic Substitution.** The study of Fe–CO fragments in diamagnetically substituted FeMoco allows for a simplified correlation between CO activation and the local electronic structure of an Fe center in the chemical environment of FeMoco. The different oxidation states in  $CO-[FeGa_6InS_9C]^{2+,1+,0}$  show a clear correspondence between the Fe electron configuration and CO activation (Figure 2a). A more reduced Fe center leads to a lower CO vibrational frequency, a shorter CO bond length, and a longer Fe–CO bond length. The CO frequency for an  $Fe^{2+}$  oxidation state ( $1884\text{ cm}^{-1}$ ,  $CO-[FeGa_6InS_9C]^{1+}$ ) is the closest to the experimental frequency for the putative terminal CO observed experimentally in FeMoco by SF-FT-IR spectroscopy (1904

$\text{cm}^{-1}$ ,  $loCO_{IR,1}$ ). An intermediate spin state is preferred for all three oxidation states after CO binding, which is in between the local high-spin state typically observed in most biological, substrate-free FeS clusters and the local low-spin state for multiple CO bound to the same Fe center.<sup>93</sup> The localized orbital analysis reveals that local spin-pairing increases  $\pi$  back bonding, which is responsible for the CO activation.

The  $CO-[Fe_2Ga_3InS_9C]^{1+}$  model shows that the second center has only a small effect on the CO activation compared to  $CO-[FeGa_6InS_9C]^{1+}$  (Figure 2a,b). However, the local spin-pairing on the CO-bound Fe center changes the sign of the coupling constant between the neighboring Fe centers. The  $\mu$ -CO binding mode in  $\mu-CO-[Fe_2Ga_3InHS_9C]^{2+}$  (Figure 2c) shows even stronger ferromagnetic coupling between Fe6 and Fe2 compared to terminal CO binding. The stability of a particular spin-coupling pattern within FeMoco is believed to depend greatly on antiferromagnetic coupling between the Fe centers.<sup>76,95</sup> CO binding might thus be expected to disrupt the energy ordering of BS determinants through local spin-pairing and by potentially replacing the bridging  $\mu-S^{2-}$  ligand.

**CO Binding to the  $E_0$  State of FeMoco.** We now turn to the full FeMoco model in the  $E_0$  state and consider the interaction between all eight magnetic centers. However, we will restrict our study to CO binding to Fe6 and Fe2 as X-ray crystallography has revealed CO binding to these atoms in the X-ray structure  $loCO_{XRD}$ . The first part of this section presents the results for a cluster model. In this model, only the cofactor and the residues with direct coordination to Fe1 and Mo are included. The remaining protein environment is replaced with a uniform dielectric continuum ( $\epsilon = 4$ ). Even though CO binding to the wild-type MoFe protein generally requires turnover conditions, we consider it important to understand how an Fe–CO bond affects the spin-coupling in the full FeMoco model and the  $E_0$  state is by far the best understood  $E_n$  state. The second part shows analogous calculations with a more realistic QM/MM model. The residues in the proximity of Fe6 and Fe2 are included in the QM region, that is, modeled with DFT, while the remaining residues are modeled with a molecular mechanics force field. By comparing the cluster model with the QM/MM model, the effects of the surrounding residues on the CO–FeMoco adduct can be discussed separately from the intrinsic electronic structure of FeMoco.

**CO Binding in a Cluster Model.** The  $E_0$  cluster model converges to stable structures with CO bound terminally to either Fe6 or Fe2, as illustrated in Figure 3a. The binding energies are calculated to be  $-6.0$  and  $-9.1\text{ kcal/mol}$ , respectively, which shows a clear preference for CO binding to Fe2. The remaining parameters related to the Fe–CO bond only differ slightly between the two binding sites (see Table 2). The calculated vibrational frequencies are  $1910$  and  $1896\text{ cm}^{-1}$  for CO bound to Fe6 and Fe2, respectively. This is in good agreement with the CO bound terminally to the diamagnetically substituted cofactor  $CO-[Fe_2Ga_3InS_9C]^{1+}$  ( $1908\text{ cm}^{-1}$ ). The lower vibrational frequency for CO bound to Fe2 ( $-14\text{ cm}^{-1}$ ) correlates with a slightly shorter Fe–CO bond length ( $-0.04\text{ Å}$ ) compared to Fe6, while the C–O bond length is nearly unchanged ( $+0.001\text{ Å}$ ).

Before CO binding, Fe6 (or Fe2) is a local high-spin center with an  $Fe^{2.5+}$  oxidation state, because it shares a minority spin electron with a neighboring metal center.<sup>18</sup> The reader is referred to Figure S2 for a schematic electronic structure of the whole, substrate-free cofactor. When binding CO, the shared electron localizes, forming an  $Fe^{2+}Fe^{3+}$  pair, where Fe6 (or

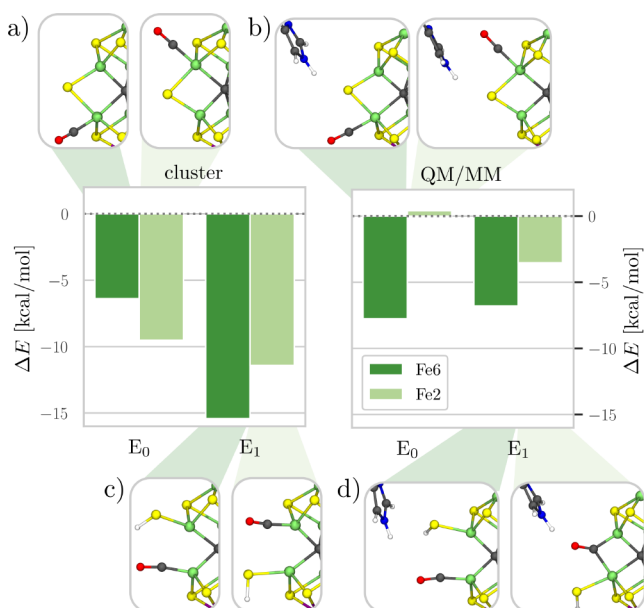


**Figure 3.** CO binding modes and binding energies for the cluster model (a,c) and the QM/MM model (b,d) for both the  $E_0$  and  $E_1$  redox states, respectively. The QM/MM model explicitly includes the protein environment such as the His195 residue. For the  $E_1$  state, the protonated S2B belt sulfide bridge opens spontaneously. When binding CO to Fe2 in the  $E_1$  QM/MM model, CO assumes the bridging position between Fe6 and Fe2. Cf. Figure S3 for substrate-free reference states and Figures S4 and S5 for other BS determinants tested.

Fe2) is the more reduced Fe center. Fe6 (or Fe2) has a local intermediate spin, with an unoccupied  $z^2$  orbital (oriented along the Fe–CO bond) and doubly occupied  $xz$  and  $yz$  orbitals (constituting the  $\pi$  back bonding). Therefore, the orbital diagram of CO– $[\text{Fe}_2\text{Ga}_3\text{InS}_9\text{C}]^{1+}$  (Figure 2b) captures the electron reorganization that happens when binding CO with the difference that the  $\text{Fe}^{2+}/\text{Fe}^{3+}$  pair is located within the respective cubane (Fe6/Fe5 and the Fe2/Fe4 pair, respectively).

In addition to the spin-pairing, the global spin-coupling pattern in FeMoco changes upon CO binding and with it the location of the mixed-valence delocalized pairs. In the

substrate-free FeMoco, the members of the BS7 class (BS7-235, BS7-247, and BS7-346) have been shown to be the lowest in energy,<sup>18,77–79</sup> which has been rationalized through the high number of antiferromagnetically aligned Fe pairs.<sup>76,95</sup> However, the study of the diamagnetically substituted cofactor showed that a terminally bound CO reduces the coupling constant between Fe centers by inducing local spin-pairing. Because the same local intermediate spin is observed for the CO-bound Fe center in the full FeMoco models, the local intermediate spin center might contribute less to the stability of the BS determinant through an antiferromagnetic alignment compared to the remaining Fe pairs. The most stable determinants after CO binding are BS10-135 and BS10-147 for CO bound to Fe6 and Fe2, respectively. BS10-135 and BS10-147 are pseudo-mirror images with respect to the plane defined by Fe6, Fe2, and CO. If the local intermediate spin center is simply disregarded when counting the number of antiferromagnetic pairs, the BS7 class loses its leading position and the BS2, BS4, BS6, BS7, BS8, and BS10 classes all have the same, maximum number of antiferromagnetic pairs. The reduced coupling strengths of the CO-bound Fe center offers an intuitive explanation as to why the lowest-energy BS determinants do not necessarily belong to the BS7 class. It further reinforces the importance of understanding the relationship between the electronic structure and the stability of BS determinants in the ligand-bound FeMoco.

The electronic structure of FeMoco in the  $E_0$  cluster model changes in a similar way when binding CO to Fe6, which is part of the Mo cubane, and to Fe2, which is part of the Fe-only cubane. However, the binding energies show a preference by about 3 kcal/mol for binding to Fe2. Because the two binding sites do not show any significant difference in the CO vibrational frequency or geometric parameters, the preference for Fe2 is related to the electronic structure of the respective cubanes. It appears that altering the electronic structure through CO binding, that is, localization of a formerly delocalized electron and/or local spin-pairing, happens more easily in the Fe-only cubane compared to the Mo cubane. This observation is possibly a consequence of the heterometal Mo, and the unusually strong Fe–Mo interaction in FeMoco<sup>96</sup> could play a role in stabilizing local high-spin Fe centers.

**Table 2.** Parameters That Characterize the CO–FeMoco Interaction in the Cluster Model and in the QM/MM Model<sup>a</sup>

		$ S_{\text{pop}} ^b$		$\Delta E^c$ [kcal/mol]	$\nu_{\text{CO}}^d$ [cm <sup>-1</sup> ]	$d_{\text{C-O}}$ [Å]	$d_{\text{Fe-CO}}$ [Å]	BS <sup>e</sup>	$M_S^f$	
		Fe6	Fe2							
E <sub>0</sub> models										
cluster	Fe6	1.56	3.19	−6.0	1910	1.158	1.760	BS10-135	0.5	
	Fe2	2.93	1.95	−9.1	1896	1.159	1.756	BS10-147	0.5	
QM/MM	Fe6	1.51	3.06	−7.8	1966	1.152	1.763	BS10-147	0.5	
	Fe2	2.96	1.81	0.4	1957	1.153	1.775	BS7-346	0.5	
E <sub>1</sub> models										
cluster	Fe6	1.07	3.22	−15.0	1821	1.171	1.735	BS10-147	0.0	
	Fe2	3.00	1.61	−11.0	1856	1.166	1.745	BS10-147	0.0	
QM/MM	Fe6	1.88	3.16	−8.3	1922	1.157	1.783	BS7-346	2.0	
	Fe6/2	2.26	2.11	−5.1	1716	1.193	2.022/1.795	BS10-147	0.0	

<sup>a</sup>The respective binding modes are shown in Figure 3 (all models), Figure 4 ( $E_0$  QM/MM), and Figure 5 ( $E_1$  QM/MM). <sup>b</sup>Spin populations are based on the Hirshfeld partitioning scheme. <sup>c</sup>The calculation of the binding energy  $\Delta E$  is explained in the Computational Details section. <sup>d</sup>Scaled vibrational frequencies. See Table S3 for unscaled frequencies. <sup>e</sup>BS refers to the spin-coupling within the broken symmetry determinant (most stable shown), with the last three integers indicating the Fe centers that hold mainly  $\beta$  spin electrons. <sup>f</sup> $M_S$  refers to the excess of  $\alpha$  spin in the BS determinant.

**CO Binding in a QM/MM Model.** In the  $E_0$  QM/MM model, placing CO in the proximity of either Fe6 or Fe2 converges to a structure with a terminally bound CO, similar to the cluster model, as shown in Figure 3b. The binding energies are  $-7.8$  and  $0.4$  kcal/mol for Fe6 and Fe2, respectively. Compared to the cluster model, CO binding is only 2 kcal/mol weaker for Fe6, but 10 kcal/mol weaker for Fe2, which indicates a strong influence of the protein environment. Indeed, the overlay of the CO-bound and substrate-free structures shows a large displacement of His195 if CO binds to Fe2 but a small displacement for Fe6 (Figure 4a,b). In order to

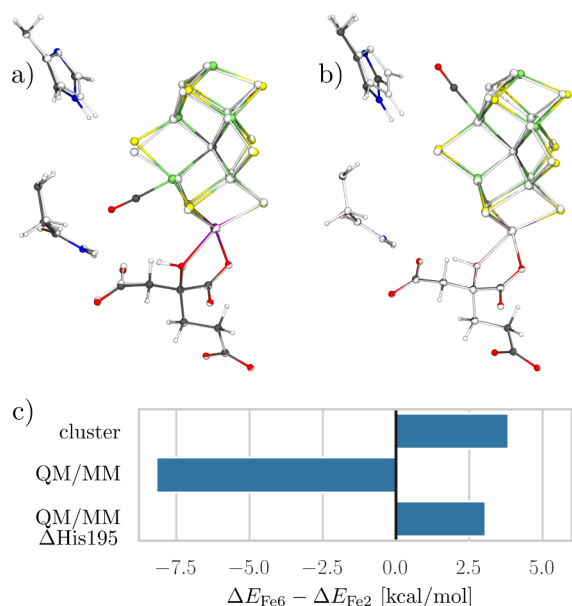


**Figure 4.** Structures of CO bound in the  $E_0$  QM/MM model to Fe6 (a) and Fe2 (b) showing also the His195 and Gln191 residues. The substrate-free model is overlaid in black and white. (c) Energy difference between the CO binding at Fe6 and at Fe2 in the cluster model, the QM/MM model, and the QM/MM model with His195 removed at a fixed geometry ( $\Delta His195$ ). Positive values indicate a preference for binding to Fe2.

verify the influence of the His residue, the binding energies were recalculated with the His residue removed from the QM/MM model at a fixed geometry (QM/MM  $\Delta His195$  model). Figure 4c compares the binding energy difference, that is, the preference of CO to bind to either Fe6 or Fe2, between the cluster model, the QM/MM model, and the QM/MM  $\Delta His195$  model. A positive value for the binding energy difference indicates a preference for Fe2. The QM/MM model has a clear preference for binding at Fe6 ( $-8.2$  kcal/mol), but the preference for Fe2 in the QM/MM  $\Delta His195$  model ( $+3.1$  kcal/mol) is nearly identical to the cluster model ( $+3.8$  kcal/mol), demonstrating the role of the His residue. The His residue forms a hydrogen bond with the belt sulfide S2B, and this bond competes with the substrate binding to Fe. The increase of the binding energy difference by 10 kcal/mol makes Fe2 an unfavorable binding site in the  $E_0$  QM/MM model, where the His–S2B hydrogen bond is still intact. This emphasizes the important role the protein environment can play in mechanistic studies of nitrogenase.

The vibrational frequency is very similar for CO bound to Fe6 ( $1966$   $cm^{-1}$ ) and to Fe2 ( $1957$   $cm^{-1}$ ). While the vibrational frequency is nearly unaffected by the 8 kcal/mol

difference in binding energy between Fe6 and Fe2, the stronger binding to Fe6 is accompanied by a  $0.01$  Å decreased Fe–CO bond length compared to Fe2. The frequency for a supposedly terminal CO observed in SF-FT-IR experiments ( $1904$   $cm^{-1}$ ,  $loCO_{IR,1}$ )<sup>38,39</sup> coincides with the calculated frequencies for the  $E_0$  cluster model ( $1910$  and  $1896$   $cm^{-1}$  for Fe6 and Fe2, respectively), but it is about  $50$   $cm^{-1}$  lower than the calculated frequencies for the  $E_0$  QM/MM model ( $1966$  and  $1957$   $cm^{-1}$  for Fe6 and Fe2, respectively). The discrepancy in the frequency between the cluster and the QM/MM model is a direct consequence of the respective descriptions of the protein environment.

The localized orbital analysis of CO-bound FeMoco in the  $E_0$  QM/MM model revealed the equivalent orbital occupation scheme as discussed for the  $E_0$  cluster model. To reiterate, the CO binding leads to the localization of a formerly delocalized electron and therefore a formal  $Fe^{2+}Fe^{3+}$  pair with a local intermediate spin on the CO-bound  $Fe^{2+}$  center. The lowest-energy determinant is BS10-147 and BS7-346 for CO bound to Fe6 and Fe2, respectively. BS7-346 is not the lowest-energy determinant in the cluster model, but as already discussed, the BS7 and BS10 classes have the same number of antiferromagnetically coupled Fe pairs when neglecting the local intermediate spin Fe center. The observation that the lowest-energy BS determinant differs between the cluster and the QM/MM model demonstrates that the explicit protein environment has a considerable influence on stabilizing certain spin-coupling patterns.

CO binding to FeMoco in the wild-type MoFe protein generally requires turnover conditions. Consistent with this observation, the calculated CO frequencies in the  $E_0$  QM/MM model ( $1966$  and  $1957$   $cm^{-1}$  for Fe6 and Fe2, respectively) are about  $50$   $cm^{-1}$  higher than the initial, experimental band at  $1904$   $cm^{-1}$  in the SF-FT-IR experiment ( $loCO_{IR,1}$ ), which suggests that a more reduced cofactor is present in the experiment. Arguably, the discrepancy is not sufficiently large to exclude the  $E_0$  redox state as the initial binding state based on the frequency alone. Nevertheless, the binding energy difference between Fe6 and Fe2 shows that ligand binding to Fe2 is strongly hindered as long as the His195 residue forms a hydrogen bond with the belt sulfide S2B.

**CO Binding to the  $E_1$  State of FeMoco.** We now turn our attention to the one-electron reduced and protonated  $E_1$  state. It has been proposed that the additional electron reduces the Fe part of the Mo cubane,<sup>20,21</sup> which is therefore expected to affect the Fe–CO interaction. The S2B belt sulfide is protonated in our model following the suggestion of a combined EXAFS and QM/MM study, but we note that the S5A position has also been proposed as a protonation site.<sup>20,22–25</sup> Similar to the  $E_0$  models, the first part of this section is dedicated to intrinsic properties of FeMoco and investigates CO binding using the cluster model. The second part focuses on the influence of the protein environment on the Fe–CO bond by repeating the calculations with the QM/MM model.

**CO Binding in a Cluster Model.** The  $E_1$  cluster model binds CO terminally at Fe6 or Fe2, as shown in Figure 3c. The binding of CO is accompanied by the spontaneous opening of the bridge formed by the protonated S2B belt sulfide between Fe6 and Fe2, resulting in a terminal CO on one Fe center and a terminal  $SH^-$  on the other. The binding energies are  $-15.0$  and  $-11.0$  kcal/mol for CO bound to Fe6 and Fe2, respectively, which makes the binding 9 and 2 kcal/mol

stronger compared to the  $E_0$  cluster model for each respective binding site. The stronger CO binding in the  $E_1$  cluster model is not surprising in view of the more reduced cofactor, but it might also be related to the opening of the  $\text{SH}^-$  bridge, reducing the coordination number at the CO-bound Fe center. CO binding is stronger for Fe6 than for Fe2, which is opposite to the preference observed in the  $E_0$  cluster model. The localized orbital analysis of the CO-bound  $E_1$  cluster model (not shown) reveals that the reduction from the  $E_0$  to the  $E_1$  redox state occurs in the respective cubane that binds CO (Fe2: Fe-only cubane; Fe6: Mo cubane). The preference for Fe6 is therefore consistent with the electronic structure of the substrate-free  $E_1$  QM/MM model, which predicts the reduction occurring in the Mo cubane rather than in the Fe-only cubane.<sup>20</sup>

The calculated CO vibrational frequencies in the  $E_1$  cluster model are 1821 and 1856  $\text{cm}^{-1}$  for Fe6 and Fe2, respectively (see Table 2). The 35  $\text{cm}^{-1}$  lower frequency for Fe6 correlates with the 4 kcal/mol stronger binding. At the same time, the C–O bond length is 0.005 Å longer for Fe6 and the Fe–CO bond length is –0.010 Å shorter. Compared to the  $E_0$  cluster model, the CO frequencies decrease by 90 and 40  $\text{cm}^{-1}$  for Fe6 and Fe2, respectively, and the Fe–CO bond lengths decrease by 0.025 and 0.010 Å, respectively, revealing a significantly more activated and more strongly bound CO in the cluster model after reduction and protonation to the  $E_1$  state.

For solution-extracted FeMoco, CO has been shown to not interact with an oxidation state that gives rise to an  $S = 3/2$  EPR signal and therefore most likely corresponds to the  $E_0$  redox state of MoFe-bound FeMoco.<sup>44</sup> However, solvated FeMoco was found to bind CO after a one-electron electrochemical reduction, where the CO–FeMoco adduct was identified by an IR band at 1835  $\text{cm}^{-1}$ . Consistent with this observation, our cluster model suggests a stronger binding in the  $E_1$  state (–15.0 to –11.0 kcal/mol) compared to the  $E_0$  state (–9.1 to –6.0 kcal/mol). Furthermore, our calculated CO frequencies for the  $E_1$  cluster model (1821 and 1856  $\text{cm}^{-1}$ ) are in good agreement with the IR band observed at 1835  $\text{cm}^{-1}$ . While the authors proposed a bridging CO, our model suggests that a terminally bound CO (with an open sulfide bridge) is also consistent with this relatively low IR frequency.

**CO Binding in a QM/MM Model.** The  $E_1$  QM/MM model predicts two distinct CO binding modes, which are shown in Figure 3d, depending on the initial binding site. When binding CO to Fe6, the CO remains as a terminal ligand on Fe6, but the protonated belt sulfide bridge opens to form a terminal  $\text{SH}^-$  on Fe2, similar to the cluster model. However, when placing CO at Fe2, the CO surprisingly assumes the bridging position ( $\mu$ -CO) between Fe6 and Fe2 during the geometry optimization. At the same time, the protonated belt sulfide bridge becomes a terminal  $\text{SH}^-$  on Fe6. The binding energies are –8.3 and –5.1 kcal/mol for the terminal and the bridging CO structure, respectively. Therefore, the binding in the  $E_1$  QM/MM model is about 7 kcal/mol weaker than in the  $E_1$  cluster model. The reason behind the less favorable binding appears to be the His195 residue. In the discussion of the  $E_1$  cluster model, binding CO to either Fe6 or Fe2 has led to an open Fe6/Fe2 bridge, that is a terminal CO and a terminal  $\text{SH}^-$  on neighboring Fe centers. However, a terminal ligand on Fe2 interferes with the His residue in the QM/MM model (cf.  $E_0$  QM/MM model in Figure 4). Even though the  $E_1$  QM/

MM model with a bridging CO does not have a terminal ligand bound to Fe2, the CO ligand assumes the less favorable bridging binding mode and thus avoids interference with the His residue. This is most likely the reason for the less strong binding in the  $E_1$  state in the QM/MM model compared to the cluster model. Furthermore, the His residue forms a 1.75 Å hydrogen bond with the CO ligand, somewhat stabilizing the bridging structure. The CO bridge is asymmetric with the Fe–CO bond lengths being 2.022 and 1.795 Å for Fe6 and Fe2, respectively.

The calculated binding energies unfortunately do not paint an unambiguous picture of CO binding to the  $E_1$  state of FeMoco. While the cluster model indicates a clearly increased binding affinity upon FeMoco reduction and protonation, the QM/MM model shows little change in the binding affinity. The protein environment in the QM/MM model appears to disfavor the structural rearrangements around Fe2 and Fe6, namely, the sulfide bridge opening, leading to weaker binding in the  $E_1$  state. It is hard to assess whether this rearrangement is similarly prohibited in the real system or whether our methodology fails to capture the conformational flexibility of the protein environment. It seems plausible that upon binding of CO to an  $E_1$  redox state (as clearly favored in the FeMoco cluster model) the protein environment may conformationally adapt to accommodate the ligand. Any sophisticated conformational change would not be accounted for in our simplistic potential energy surface calculations that are biased toward unbound FeMoco and may require more elaborate free-energy simulations, which are outside the scope of this study.

The calculated CO vibrational frequencies for the  $E_1$  QM/MM model are 1922 and 1716  $\text{cm}^{-1}$  for the terminal and the bridging binding mode, respectively (see Table 2). The frequency for the terminal CO bound to Fe6 is about 45  $\text{cm}^{-1}$  lower compared to the  $E_0$  QM/MM model. This reduction in frequency correlates with an increase in the C–O bond length of 0.004 Å. However, the Fe–CO bond length is 0.02 Å longer in the  $E_1$  QM/MM model, despite the more activated CO. Notably, the frequency for the bridging CO is 100–250  $\text{cm}^{-1}$  lower than all CO-bound QM/MM models discussed so far, allowing for a clear distinction between a terminal and a bridging CO.

The electron distribution in the two CO binding modes observed in the  $E_1$  QM/MM model is shown in Figure 5. For the terminally bound CO (Figure 5a), the additional electron added in the  $E_0$  to  $E_1$  redox event localizes on Fe6 and contributes directly to the  $\pi$  back bonding. In contrast to the  $E_0$  models, CO binding does not induce spin-pairing neither through a local spin flip nor through the localization of a delocalized electron. The CO-bound Fe center in the  $E_1$  QM/MM model therefore remains a local high-spin center. Nevertheless, according to the QM/MM model, the activation of CO is stronger in the  $E_1$  state compared to the  $E_0$  state, even though only three and not four electrons are involved in the  $\pi$  back bonding.

For the bridging CO (Figure 5b), the lowest-energy determinant is BS10-147, and Fe6 and Fe2 are ferromagnetically aligned, which is also the favorable alignment according to the coupling constant in the diamagnetically substituted cofactor  $\mu$ -CO– $[\text{Fe}_2\text{Ga}_3\text{InHS}_9\text{C}]^{2+}$  ( $J = +34 \text{ cm}^{-1}$ ). A total of seven Fe-based orbitals have a strong overlap with the CO  $\pi^*$  orbitals (indicated by dashed circles). Using the orbital labels introduced previously for the diamagnetically substituted cofactor (Figure 2c), the delocalized orbital is the bonding

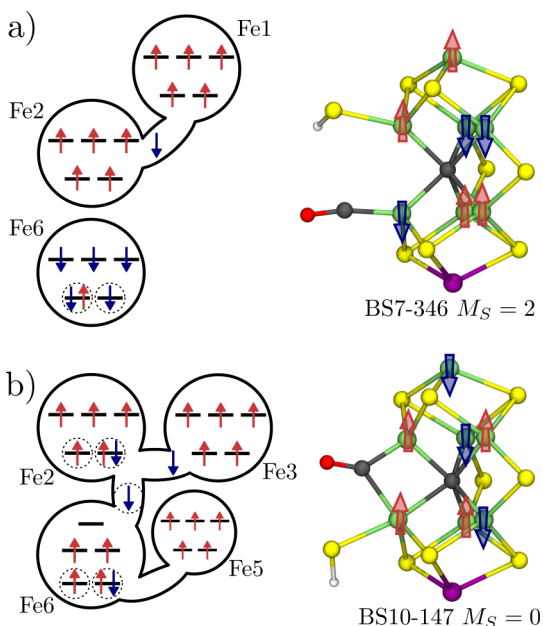


**Figure 5.** Two CO binding modes in the  $E_1$  QM/MM model featuring (a) a terminal CO and a terminal  $\text{SH}^-$  and (b) a bridging CO ( $\mu\text{-CO}$ ) and a terminal  $\text{SH}^-$ . The orbital diagrams show the electron distribution at Fe6 and Fe2 and the involvement of neighboring Fe centers. The dashed circles highlight orbitals that significantly overlap with CO. The large arrows in the FeMoco structures show the local majority spin for each Fe center and therefore visualize the BS determinant.

linear combination of the out-of-plane  $xy$  orbitals on Fe6 and Fe2. The doubly occupied orbitals on Fe6 and Fe2, respectively, are the in-plane  $yz$  orbitals, while the two singly occupied orbitals are the out-of-plane  $xy$  orbitals. However, a more detailed comparison of the electronic structures of the  $\mu\text{-CO}$ -bound  $E_1$  QM/MM model, and  $\mu\text{-CO}$ - $[\text{Fe}_2\text{Ga}_3\text{InHS}_9\text{C}]^{2+}$  reveals some differences: (i) Fe2 remains a local high-spin center in the full cofactor model but has a local intermediate spin in  $\mu\text{-CO}$ - $[\text{Fe}_2\text{Ga}_3\text{InHS}_9\text{C}]^{2+}$ . (ii) The full cofactor model features a delocalized electron between Fe6 and Fe2, the electrons in  $\mu\text{-CO}$ - $[\text{Fe}_2\text{Ga}_3\text{InHS}_9\text{C}]^{2+}$  are localized on either Fe6 or Fe2. (iii) The orbitals that are preferentially doubly occupied are the in-plane  $yz$  orbital for the full cofactor model but out-of-plane  $xy$  for  $\mu\text{-CO}$ - $[\text{Fe}_2\text{Ga}_3\text{InHS}_9\text{C}]^{2+}$ . These differences can be attributed to the spin–spin interaction between Fe6/Fe2 and the remaining metal centers in FeMoco. For example, (i) illustrates the competition between a local intermediate spin, which strengthens the Fe–CO bond through spin-pairing and a local high-spin, which contributes to the stability of the BS determinant, because a high-spin Fe center exhibits stronger antiferromagnetic coupling with its neighbors.

An interesting observation is related to the local spin state and the coordination number of the Fe centers. All CO-bound Fe centers in the  $E_0$  models exhibit a local intermediate spin. For the  $E_1$  models, the only intermediate spin state is observed in the bridging CO structure, in which Fe6 is ligated by both  $\mu\text{-CO}$  and a terminal  $\text{SH}^-$  (Figure 5b). Local intermediate spin states apparently arise when five ligands are bound to an Fe center resulting in an approximately trigonal-bipyramidal coordination. In contrast, local high-spin states are observed for an approximately tetrahedral environment, even if CO is part of the coordinating ligands. Therefore, the appearance of a

local intermediate spin appears to be related more to the local geometry and the coordination number than to the nature of the ligand. Considering the competition between on-site spin-pairing and inter-site spin-coupling discussed during the comparison of  $\mu\text{-CO}$ - $[\text{Fe}_2\text{Ga}_3\text{InHS}_9\text{C}]^{2+}$  with the full cofactor model, any pentacoordinated Fe center might be unfavorable for FeMoco because its potential local intermediate spin may affect the antiferromagnetic coupling to the remaining metal centers. This important mechanistic detail might be translated to the binding of other substrates, such as acetylene or  $\text{N}_2$ .

The calculated vibrational frequencies for terminal and bridging CO in the  $E_1$  QM/MM model (1922 and 1716  $\text{cm}^{-1}$ , respectively) are in good agreement with the bands corresponding to  $\text{loCO}_{\text{IR},1}$  and  $\text{loCO}_{\text{IR},2}$  in the SF-FT-IR experiment (1904 and 1715  $\text{cm}^{-1}$ , respectively), indicating the relevance of these coordination geometries to the mechanism of CO inhibition.<sup>38</sup> The first, transient band ( $\text{loCO}_{\text{IR},1}$ ) has been shown to shift by 11  $\text{cm}^{-1}$  to lower frequencies with the mutation of the Val70 residue to Ile.<sup>40</sup> The same mutation in our  $E_1$  QM/MM model resulted in a decrease of the calculated 1922  $\text{cm}^{-1}$  frequency by 17  $\text{cm}^{-1}$ , further supporting the assignment of a terminal CO at Fe6 to the  $\text{loCO}_{\text{IR},1}$  species. Furthermore, the calculated frequency of the bridging CO in the  $E_1$  QM/MM model agrees well with the band observed in  $\text{loCO}_{\text{IR},2}$ . With the apparent necessity of the His195 residue stabilizing the bridging CO, the Fe6/Fe2 pair is the most probable binding site for the bridging CO, consistent with the CO-bound X-ray structure  $\text{loCO}_{\text{XRD}}$ . Admittedly, the CO- $[\text{FeGa}_6\text{InS}_9\text{C}]^0$  model suggests that frequencies below 1800  $\text{cm}^{-1}$  could be possible for a terminal CO bound to an  $\text{Fe}^{1+}$  center in the chemical environment of FeMoco (cf. Table 1). However, the local oxidation state  $\text{Fe}^{1+}$  was not observed in any of the full cofactor models and appears rather unlikely, considering the flexible charge redistribution within the cofactor, which is possibly facilitated by the highly covalent  $\mu_6\text{-C}^{4-}$  center.<sup>64</sup>

In the SF-FT-IR experiment, the 1904  $\text{cm}^{-1}$  band ( $\text{loCO}_{\text{IR},1}$ ) completely converts to the 1715  $\text{cm}^{-1}$  band ( $\text{loCO}_{\text{IR},2}$ ) within minutes, suggesting that the latter corresponds to a thermodynamic sink. The energies of the terminal and the bridging CO structure in the  $E_1$  QM/MM model lie merely 3 kcal/mol apart (terminal lower in energy), which does not indicate a preference for either binding mode. The CO-bound X-ray structure ( $\text{loCO}_{\text{XRD}}$ ) also features a bridging CO between Fe6 and Fe2, but the S2B belt sulfide is missing completely, suggesting sulfide dissociation as a logical pathway for the complete conversion to a bridging CO. The dissociation of  $\text{SH}^-$  from the CO-bound  $E_1$  QM/MM model is energetically unfavorable, but there are at least two effects that need to be considered in this context. First, the change in entropy is an important contribution to the dissociation free energy, which is not captured by our potential energy surface calculations. Second, the lability of the belt sulfide has been demonstrated for protein-bound FeMoco in which the S2B position was selectively substituted with Se.<sup>97</sup> Here, in the CO-inhibited form (Se analogue of  $\text{loCO}_{\text{XRD}}$ ), Se has been shown to further replace the other two belt sulfides S3A and S5A. The high mobility of Se during CO inhibition might indicate a more complex pathway for the sulfide expulsion from the cofactor *via* the S3A and S5A belt positions rather than the simple dissociation of  $\text{SH}^-$  or  $\text{H}_2\text{S}$  from the S2B belt position. To test such a mechanism would require the simultaneous and accurate treatment of the electronic structure of FeMoco and

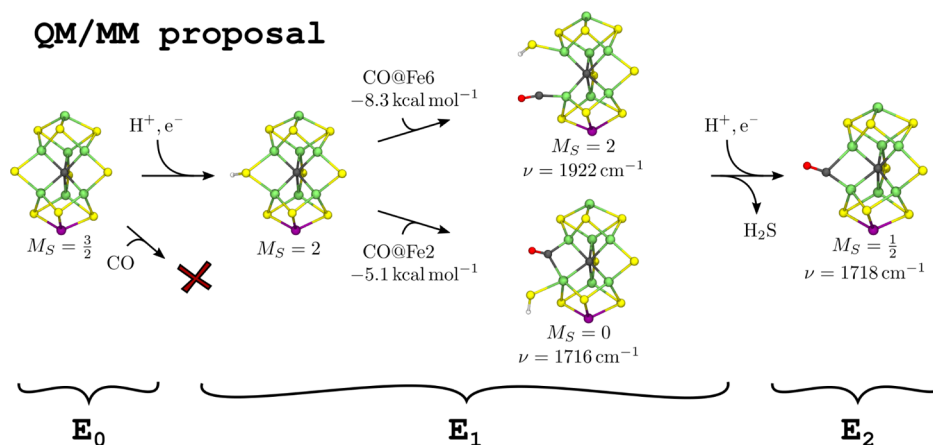


**Figure 6.** Mechanism for the binding of a single CO molecule to FeMoco based on QM/MM calculations. In the  $E_0$  state, CO binding is found to be unlikely in the resting state model, consistent with the experiment. In the  $E_1$  state, the protonated Fe2/Fe6 sulfide bridge spontaneously opens upon CO binding. Two stable structures, one featuring a terminal and one a bridging CO, lie close in energy, and their calculated vibrational frequencies agree well with the experimentally observed SF-FT-IR bands at 1904 and 1715  $\text{cm}^{-1}$  ( $\text{loCO}_{\text{IR},1}$  and  $\text{loCO}_{\text{IR},2}$ , respectively). Alternatively, an additional protonation/reduction event to the  $E_2$  redox state might be necessary to dissociate  $\text{SH}^-$  from the cofactor, as observed in the X-ray structure ( $\text{loCO}_{\text{XRD}}$ ). In the QM/MM model, this leads to a semi-bridging CO with a calculated frequency also consistent with the SF-FT-IR species  $\text{loCO}_{\text{IR},2}$  and an  $M_S$  value consistent with the  $S = 1/2$  EPR signal  $\text{loCO}_{\text{EPR}}$ .

the conformational flexibility of the protein environment in a combined DFT/molecular dynamics (MD) simulation, which is beyond the scope of this study. Alternatively, sulfide dissociation might not happen in the  $E_1$  redox state after all, but additional protonation and reduction might be necessary to dissociate the belt sulfide. To summarize, the calculated frequencies in the CO-bound  $E_1$  QM/MM model are consistent with the SF-FT-IR bands under low CO pressures ( $\text{loCO}_{\text{IR},1}$  and  $\text{loCO}_{\text{IR},2}$ ), but it neither captures the conversion of a supposedly terminal to a bridging CO suggested by the time-dependence of the SF-FT-IR bands nor the dissociation of the belt sulfide indicated by the CO-bound X-ray structure ( $\text{loCO}_{\text{XRD}}$ ).

Henthorn *et al.* probed the electronic structure of CO-bound FeMoco in the MoFe protein through Se substitution and Se K-edge high-energy resolution fluorescence detected (HERFD) XAS.<sup>64</sup> Their results are consistent with the Fe3/Fe4/Fe5/Fe7 centers being more oxidized after CO binding compared to the resting state MoFe protein and, therefore, the electron density appears to shift toward the CO binding site. This experimentally observed redox rearrangement for Se-substituted FeMoco is not apparent in the localized orbitals of our CO-bound  $E_1$  QM/MM model, where the oxidation state of the Fe3/Fe4/Fe5/Fe7 centers is equivalent to the  $E_0$  QM/MM model. In this context, it should be noted that the spatially resolved anomalous dispersion (SpReAD) refinement of the Fe K-edge XAS of the resting state MoFe protein supports a rather localized electron distribution in FeMoco, with Fe3/Fe7 being more oxidized compared to Fe2/Fe4/Fe5/Fe6.<sup>19</sup> Meanwhile, the Fe2/Fe3 and Fe6/Fe7 pairs have a formal  $\text{Fe}^{2.5+}$  oxidation state according to the localized orbital analysis in the  $E_0$  QM/MM BS7-235 model.<sup>18</sup> The link between DFT models and experiment is further complicated by the presence of two other low-energy determinants (BS7-346 and BS7-247) in the calculations that change the location of those mixed-valence pairs, meaning that experiments may be measuring a complex average of multiple electronic configurations, making comparison with a single BS determinant insufficient. Additionally vibronic coupling at experimental temperatures may serve to localize electrons in FeMoco.

Therefore, the BS-DFT approach is likely insufficient to treat all aspects of the complex electronic structure of FeMoco. Recent advances have enabled the application of multi-configurational quantum chemical methods to systems that have the size and complexity of FeMoco.<sup>98–100</sup> It remains to be seen how far these methods can be pushed in the future toward quantitative accuracy.

**Proposed CO Binding Mechanism.** Finally, we would like to propose the mechanism in Figure 6 for the binding of CO to FeMoco based on our QM/MM model. CO binding to the wild-type MoFe protein generally requires turnover conditions suggesting one or multiple binding  $E_n$  states with  $n > 0$ . Agreeing with this observation, the calculated terminal CO frequencies in the  $E_0$  QM/MM model are 50–60  $\text{cm}^{-1}$  higher than the initial, transient SF-FT-IR band at 1904  $\text{cm}^{-1}$  ( $\text{loCO}_{\text{IR},1}$ ) suggesting that a more reduced CO-bound FeMoco gives rise to this IR species. The  $E_1$  QM/MM model features both a terminal and a bridging CO bound to FeMoco, and the calculated CO frequencies, 1922 and 1716  $\text{cm}^{-1}$ , are consistent with the initial and final SF-FT-IR bands observed under turnover conditions and low CO pressures at 1904 and 1715  $\text{cm}^{-1}$ , respectively ( $\text{loCO}_{\text{IR},1}$  and  $\text{loCO}_{\text{IR},2}$ ). In both cases, CO binding led to the spontaneous opening of the protonated S2B belt sulfide bridge. However, the CO-bound X-ray structure ( $\text{loCO}_{\text{XRD}}$ ) indicates that S2B eventually dissociates from FeMoco, and the conversion of the SF-FT-IR species  $\text{loCO}_{\text{IR},1}$  to  $\text{loCO}_{\text{IR},2}$  suggests that the latter bridging CO species is a thermodynamic sink. Our QM/MM model does not support sulfide dissociation in the form of  $\text{SH}^-$  to occur at the  $E_1$  redox level. Starting with an elongated Fe6–SH<sup>−</sup> bond length of 3.3 Å, the geometry optimization reconverged to the same SH<sup>−</sup>-bound structure. Furthermore, protonation of SH<sup>−</sup> from homocitrate also did not lead to spontaneous sulfide dissociation. With an initially elongated FeMoco–H<sub>2</sub>S bond the geometry optimization converged to a structure with H<sub>2</sub>S loosely bound in between homocitrate and Gln191, but more than 30 kcal/mol higher in energy. Exploring the dissociation pathways further would most likely require the inclusion of thermodynamic effects in a DFT/MD simulation, which is beyond the scope of this study. Nevertheless, the  $E_1$  redox state

is an even-electron state and can therefore not be responsible for the  $S = 1/2$  EPR signal ( $\text{loCO}_{\text{EPR}}$ ), which is detected in the sample of the CO-bound X-ray structure ( $\text{loCO}_{\text{XRD}}$ ). This makes the odd-electron  $E_2$  state a plausible candidate for the EPR signal  $\text{loCO}_{\text{EPR}}$ . Therefore, we will briefly explore the properties of a CO-bound  $E_2$  state in a QM/MM model in which S2B is missing.

We assume for our  $E_2$  QM/MM model that the additional proton is used to dissociate the S2B belt sulfide from FeMoco in the form of  $\text{H}_2\text{S}$ , because a quantum refinement study of the X-ray structure  $\text{loCO}_{\text{XRD}}$  suggests that CO-bound FeMoco is not protonated,<sup>52</sup> and therefore have removed  $\text{H}_2\text{S}$  completely from the model. CO in the  $E_2$  QM/MM model forms a semi-bridge between Fe6 and Fe2 (see Figure 6) with Fe–CO bond lengths being 1.765 and 2.250 Å, respectively. The hydrogen bond between CO and His195 is 1.88 Å and therefore only slightly longer (0.13 Å) than in the  $\mu$ -CO  $E_1$  QM/MM model. The lowest-energy BS determinant for this binding mode is BS7-235, rather than BS10-147, suggesting that the ferromagnetic alignment of Fe6 and Fe2 is less important with a semi-bridging CO compared to the bridging CO in the  $E_1$  QM/MM model. The  $M_S = 1/2$  value of the determinant is consistent with the  $S = 1/2$  EPR signal under low CO pressures ( $\text{loCO}_{\text{EPR}}$ ). Interestingly, the calculated frequency of the semi-bridging CO is with  $1718\text{ cm}^{-1}$  virtually identical to the bridging CO in the  $E_1$  model ( $1716\text{ cm}^{-1}$ ). As a consequence, both the  $E_1$  and the  $E_2$  QM/MM model are consistent with the frequency observed for the supposedly bridging CO in the SF-FT-IR experiment under low CO pressures ( $\text{loCO}_{\text{IR},2}$ ). We wish to emphasize again that this brief exploration merely illustrates that the calculated CO frequencies are similar for an  $E_1$  model with  $\text{SH}^-$  bound and an  $E_2$  model with  $\text{SH}^-$  removed. A thorough treatment of any FeMoco redox state requires an in-depth analysis of the electronic structure.

Even though the three classes of nitrogenase are believed to reduce  $\text{N}_2$  via one unified mechanism,<sup>7</sup> they exhibit significant differences with respect to CO. Most importantly, in the wild-type Mo nitrogenase, CO merely acts as an inhibitor to  $\text{N}_2$  reduction, while V and Fe nitrogenases reduce CO to hydrocarbons.<sup>15</sup> On the other hand, Val70 mutants of Mo nitrogenase have the ability to reduce CO, which showcases the crucial role of the protein environment in addition to the electronic structure of the cofactor. It has been reported for V nitrogenase that it can bind CO without turnover conditions,<sup>11,12</sup> which could be a result of the Fe centers in the V nitrogenase resting state being more reduced compared to Mo nitrogenase.<sup>18,96,101</sup> However, some controversy exists around this observation and even the nature of the V nitrogenase resting state.<sup>54,102</sup> Nevertheless, CO binding to V nitrogenase has been shown to elicit similar EPR signals as in Mo nitrogenase ( $\text{loCO}_{\text{EPR}}$  and  $\text{hiCO}_{\text{EPR}}$ ),<sup>11,12</sup> as well as analogous X-ray structures ( $\text{loCO}_{\text{XRD}}$  and  $\text{hiCO}_{\text{XRD}}$ ).<sup>54,103</sup>

In connection with the X-ray structures, it has been proposed that an  $E_2$  state containing a hydride bridging Fe6 and Fe2 is a prerequisite to CO binding.<sup>54</sup> Elimination of  $\text{H}_2$  would then lead to an  $E_0$  redox state with CO bridging Fe6 and Fe2 and supposedly the redox state of the X-ray structure  $\text{loCO}_{\text{XRD}}$ . Preliminary calculations for an  $E_0$  QM/MM model without the bridging sulfide suggest that the CO frequency is more than  $100\text{ cm}^{-1}$  higher compared to the  $E_2$  QM/MM model, a consequence of the two-electron oxidation. The calculated CO frequency of the  $E_2$  QM/MM model is close to the experimental SF-FT-IR band  $\text{loCO}_{\text{IR},2}$ . This once more

emphasizes the importance of applying multiple and ideally orthogonal experimental techniques when characterizing a given nitrogenase species.

## CONCLUSIONS

Herein, we have systematically investigated which oxidation and protonation state of FeMoco is required for CO binding. Generally, binding CO to FeMoco in the wild-type MoFe protein requires turnover conditions, while binding CO to solution-extracted FeMoco requires electrochemical reduction to an  $E_1$ -equivalent cofactor charge state. We have calculated the CO binding energy in the  $E_0$  and  $E_1$  redox states using both a cluster model and a QM/MM model (see Table 2 and Figure 3). The  $E_0$  QM/MM model weakly binds CO at Fe6, but the binding energy ( $\Delta E = -7.8\text{ kcal/mol}$ ) might be insufficient to overcome the primarily translational entropic penalty associated with the complex formation, which is typically estimated at around  $10\text{ kcal/mol}$ , based on gas phase statistical mechanics.<sup>104</sup> The  $E_1$  cluster model clearly binds CO ( $\Delta E = -15.0\text{ kcal/mol}$ ), but for the  $E_1$  QM/MM model ( $\Delta E = -8.3\text{ kcal/mol}$ ) the binding is only slightly stronger as compared to  $E_0$ . However, with the protein environment in the QM/MM model being biased toward a substrate-free FeMoco, the surrounding residues may not have the necessary conformational flexibility during a simple potential energy surface calculation to accommodate the structural rearrangements such as the opening of the S2B belt sulfide bridge in the context of CO binding. A more complex simulation that includes the dynamics of the protein environment may be needed to give a realistic binding affinity estimate. On the other hand, the scaled calculated vibrational frequency for a terminal CO bound in the  $E_1$  QM/MM model ( $1922\text{ cm}^{-1}$ ) is in good agreement with the initially observed experimental SF-FT-IR species  $\text{loCO}_{\text{IR},1}$  ( $1904\text{ cm}^{-1}$ )<sup>38</sup> Therefore, CO might bind already to the  $E_1$  state.

Furthermore, we have compared Fe6 and Fe2 as potential CO binding sites because the X-ray structure  $\text{loCO}_{\text{XRD}}$  shows CO bridging Fe6 and Fe2. In the  $E_1$  cluster model, binding to Fe6 is about  $4\text{ kcal/mol}$  more favorable compared to Fe2, in line with the more reduced Mo cubane in the substrate-free  $E_1$  redox state.<sup>20</sup> In the  $E_1$  QM/MM model, the scaled calculated vibrational frequency of a terminal CO bound to Fe6 ( $1922\text{ cm}^{-1}$ ) agrees well with the  $\text{loCO}_{\text{IR},1}$  species ( $1904\text{ cm}^{-1}$ ), which is the initially appearing species in the SF-FT-IR experiment. Also, the CO frequency of the supposedly  $\text{loCO}_{\text{IR},1}$  species has been shown to decrease by  $11\text{ cm}^{-1}$  in Val70→Ile mutants,<sup>40</sup> and the same mutation results in a similar decrease ( $17\text{ cm}^{-1}$ ) in the  $E_1$  QM/MM model. In particular, the His195 residue disfavors binding to Fe2, as can be seen by the about  $10\text{ kcal/mol}$  stronger binding to Fe6 as compared to Fe2 for CO in the  $E_0$  QM/MM model (cf. Figure 4). Therefore, the initial CO binding site is most likely Fe6.

In order to separate the influence of the protein environment on CO binding from the intrinsic properties of the cofactor, we have compared a FeMoco cluster model with a QM/MM model. In addition to shielding Fe2 from initial substrate binding, the His195 residue forms a hydrogen bond with the bridging CO in the  $E_1$  QM/MM model (see Figure 3d). In the  $E_1$  cluster model, a terminal CO is the lowest-energy binding mode; therefore, the His195 residue appears to be explicitly responsible for stabilizing a bridging CO motif. The scaled calculated frequency of the bridging CO in the  $E_1$  QM/MM model ( $1716\text{ cm}^{-1}$ ) is consistent with the final band

at 1715  $\text{cm}^{-1}$  observed in the SF-FT-IR experiment under low CO pressures. Furthermore, the CO-bound X-ray structure  $\text{loCO}_{\text{XRD}}$  also features a bridging CO with a hydrogen bond to His195.

The CO-bound  $E_1$  QM/MM model displays two distinct binding modes: a terminal CO at Fe6 and a CO bridging Fe6 and Fe2. The scaled calculated CO vibrational frequencies (1922 and 1716  $\text{cm}^{-1}$ , respectively) are in good agreement with the experimental SF-FT-IR species  $\text{loCO}_{\text{IR},1}$  and  $\text{loCO}_{\text{IR},2}$  (1904 and 1715  $\text{cm}^{-1}$ , respectively).<sup>38</sup> However, the two binding modes are close in energy (3 kcal/mol, terminal more favorable), which is not consistent with the complete conversion of  $\text{loCO}_{\text{IR},1}$  to  $\text{loCO}_{\text{IR},2}$  observed under turnover conditions. Alternatively, CO bound to an  $E_2$  QM/MM model (with the S2B belt sulfide removed to be consistent with the X-ray structure  $\text{loCO}_{\text{XRD}}$ ) has virtually the same scaled calculated frequency (1718  $\text{cm}^{-1}$ ) as CO bound to the  $E_1$  QM/MM model, which suggests that both oxidation states would not necessarily be distinguishable in an IR experiment. The  $S = 1/2$  signal in  $\text{loCO}_{\text{EPR}}$  can only arise from an odd-electron redox state such as  $E_2$ . Therefore, a parallel IR/EPR study of CO binding to FeMoco could clarify whether the appearance of the 1715  $\text{cm}^{-1}$  band in  $\text{loCO}_{\text{IR},2}$  coincides with the  $S = 1/2$  signal in  $\text{loCO}_{\text{EPR}}$ .

In our  $E_1$  QM/MM model, CO binding leads to the spontaneous opening of the protonated S2B belt sulfide bridge to give a terminal  $\text{SH}^-$  ligand. Since practically no alternative substrates or inhibitors are known to interact with the wild-type MoFe protein in the  $E_0$  state, we speculate that this type of ligand-bound geometry in the  $E_1$  redox state may represent the initial mode of binding for various other substrates/inhibitors as well. A terminal  $\text{SH}^-$  has also been proposed in other computational studies, for example, as an intermediate during acetylene reduction<sup>105</sup> and as an intermediate of the more complicated  $\text{N}_2$  reduction pathway.<sup>63,106,107</sup> The complete dissociation of the S2B belt sulfide is known to occur as part of CO inhibition from X-ray structures.<sup>46,47</sup> It remains unclear whether sulfide loss from the cofactor is a prerequisite for the catalytic activity of Mo nitrogenase, as has been discussed in the literature, or whether it is simply a byproduct of CO inhibition.<sup>108–111</sup>

## ■ ASSOCIATED CONTENT

### SI Supporting Information

The Supporting Information is available free of charge at <https://pubs.acs.org/doi/10.1021/acs.inorgchem.1c02649>.

Example input files for diamagnetically substituted cofactors in Figure 2 (folder: diamagnetic); xyz files for substrate-free models and CO-bound models in Figure 3 (folder: geometries, for QM/MM models both the QM and the active region are included)(ZIP)

QM region used in the QM/MM model for MoFe protein; electronic structure of the substrate-free cofactor; energies of other BS determinants; ChemShell setup; localized orbital analysis; coupling constants; metal–metal distance; vibrational frequencies; and Hirshfeld population analysis (PDF)

## ■ AUTHOR INFORMATION

### Corresponding Authors

Ragnar Bjornsson – Max Planck Institute for Chemical Energy Conversion, 45470 Mülheim an der Ruhr, Germany;

[orcid.org/0000-0003-2167-8374](https://orcid.org/0000-0003-2167-8374);  
Email: [ragnar.bjornsson@cec.mpg.de](mailto:ragnar.bjornsson@cec.mpg.de)

Serena DeBeer – Max Planck Institute for Chemical Energy Conversion, 45470 Mülheim an der Ruhr, Germany;

[orcid.org/0000-0002-5196-3400](https://orcid.org/0000-0002-5196-3400);  
Email: [serena.debeer@cec.mpg.de](mailto:serena.debeer@cec.mpg.de)

Frank Neese – Max-Planck-Institut für Kohlenforschung, 45470 Mülheim an der Ruhr, Germany; [orcid.org/0000-0003-4691-0547](https://orcid.org/0000-0003-4691-0547); Email: [neese@kofo.mpg.de](mailto:neese@kofo.mpg.de)

### Author

Nico Spiller – Max-Planck-Institut für Kohlenforschung, 45470 Mülheim an der Ruhr, Germany; [orcid.org/0000-0002-6293-4867](https://orcid.org/0000-0002-6293-4867)

Complete contact information is available at:

<https://pubs.acs.org/10.1021/acs.inorgchem.1c02649>

### Funding

Open access funded by Max Planck Society.

### Notes

The authors declare no competing financial interest.

## ■ ACKNOWLEDGMENTS

The authors thank the Max Planck Society, the DFG SPP 1927 “Iron Sulfur for Life” [projects DE 1877/1-1 (S.D.) and NE 690/16-1 (F.N.)], the University of Iceland Research Fund and the IRF [grants 141218051 and 162880051 (R.B.)], and the IMPRS-RECHARGE (N.S.) for funding.

## ■ REFERENCES

- (1) Burgess, B. K.; Lowe, D. J. Mechanism of Molybdenum Nitrogenase. *Chem. Rev.* **1996**, *96*, 2983–3012.
- (2) Lancaster, K. M.; Roemelt, M.; Ettenhuber, P.; Hu, Y.; Ribbe, M. W.; Neese, F.; Bergmann, U.; DeBeer, S. X-ray Emission Spectroscopy Evidences a Central Carbon in the Nitrogenase Iron-Molybdenum Cofactor. *Science* **2011**, *334*, 974–977.
- (3) Spatzal, T.; Aksoyoglu, M.; Zhang, L.; Andrade, S. L. A.; Schleicher, E.; Weber, S.; Rees, D. C.; Einsle, O. Evidence for Interstitial Carbon in Nitrogenase FeMo Cofactor. *Science* **2011**, *334*, 940.
- (4) Thorneley, R. N. F.; Lowe, D. J. The mechanism of *Klebsiella pneumoniae* nitrogenase action. Pre-steady-state kinetics of an enzyme-bound intermediate in  $\text{N}_2$  reduction and of  $\text{NH}_3$  formation. *Biochem. J.* **1984**, *224*, 887–894.
- (5) Hoffman, B. M.; Lukoyanov, D.; Yang, Z.-Y.; Dean, D. R.; Seefeldt, L. C. Mechanism of Nitrogen Fixation by Nitrogenase: The Next Stage. *Chem. Rev.* **2014**, *114*, 4041–4062.
- (6) Eady, R. R. Structure–Function Relationships of Alternative Nitrogenases. *Chem. Rev.* **1996**, *96*, 3013–3030.
- (7) Harris, D. F.; Lukoyanov, D. A.; Kallas, H.; Trncik, C.; Yang, Z.-Y.; Compton, P.; Kelleher, N.; Einsle, O.; Dean, D. R.; Hoffman, B. M.; Seefeldt, L. C. Mo-, V-, and Fe-Nitrogenases Use a Universal Eight-Electron Reductive-Elimination Mechanism To Achieve  $\text{N}_2$  Reduction. *Biochemistry* **2019**, *58*, 3293–3301.
- (8) Van Stappen, C.; Decamps, L.; Cutsail, G. E.; Bjornsson, R.; Henthorn, J. T.; Birrell, J. A.; DeBeer, S. The Spectroscopy of Nitrogenases. *Chem. Rev.* **2020**, *120*, 5005–5081.
- (9) Hwang, J. C.; Chen, C. H.; Burris, R. H. Inhibition of nitrogenase-catalyzed reductions. *Biochim. Biophys. Acta, Bioenerg.* **1973**, *292*, 256–270.
- (10) McLean, P. A.; True, A.; Nelson, M. J.; Lee, H.-I.; Hoffman, B. M.; Orme-Johnson, W. H. Effects of substrates (methyl isocyanide,  $\text{C}_2\text{H}_2$ ) and inhibitor (CO) on resting-state wild-type and NifV–*Klebsiella pneumoniae* MoFe proteins. *J. Inorg. Biochem.* **2003**, *93*, 18–32.

- (11) Lee, C. C.; Fay, A. W.; Weng, T.-C.; Krest, C. M.; Hedman, B.; Hodgson, K. O.; Hu, Y.; Ribbe, M. W. Uncoupling binding of substrate CO from turnover by vanadium nitrogenase. *Proc. Natl. Acad. Sci.* **2015**, *112*, 13845–13849.
- (12) Lee, C. C.; Wilcoxon, J.; Hiller, C. J.; Britt, R. D.; Hu, Y. Evaluation of the Catalytic Relevance of the CO-Bound States of V-Nitrogenase. *Angew. Chem., Int. Ed.* **2018**, *57*, 3411–3414.
- (13) Lee, C. C.; Hu, Y.; Ribbe, M. W. Vanadium Nitrogenase Reduces CO. *Science* **2010**, *329*, 642.
- (14) Yang, Z.-Y.; Dean, D. R.; Seefeldt, L. C. Molybdenum Nitrogenase Catalyzes the Reduction and Coupling of CO to Form Hydrocarbons\*. *J. Biol. Chem.* **2011**, *286*, 19417–19421.
- (15) Harris, D. F.; Jimenez-Vicente, E.; Yang, Z.-Y.; Hoffman, B. M.; Dean, D. R.; Seefeldt, L. C. CO as a substrate and inhibitor of H<sup>+</sup> reduction for the Mo-, V-, and Fe-nitrogenase isozymes. *J. Inorg. Biochem.* **2020**, *213*, 111278.
- (16) Münck, E.; Rhodes, H.; Orme-Johnson, W. H.; Davis, L. C.; Brill, W. J.; Shah, V. K. Nitrogenase. VIII. Mössbauer and EPR spectroscopy. The MoFe protein component from *Azotobacter vinelandii* OP. *Biochim. Biophys. Acta, Protein Struct.* **1975**, *400*, 32–53.
- (17) Bjornsson, R.; Neese, F.; DeBeer, S. Revisiting the Mössbauer Isomer Shifts of the FeMoco Cluster of Nitrogenase and the Cofactor Charge. *Inorg. Chem.* **2017**, *56*, 1470–1477.
- (18) Benediktsson, B.; Bjornsson, R. QM/MM Study of the Nitrogenase MoFe Protein Resting State: Broken-Symmetry States, Protonation States, and QM Region Convergence in the FeMoco Active Site. *Inorg. Chem.* **2017**, *56*, 13417–13429.
- (19) Spatzal, T.; Schlesier, J.; Burger, E.-M.; Sippel, D.; Zhang, L.; Andrade, S. L. A.; Rees, D. C.; Einsle, O. Nitrogenase FeMoco investigated by spatially resolved anomalous dispersion refinement. *Nat. Commun.* **2016**, *7*, 10902.
- (20) Van Stappen, C.; Thorhallsson, A. T.; Decamps, L.; Bjornsson, R.; DeBeer, S. Resolving the structure of the E1 state of Mo nitrogenase through Mo and Fe K-edge EXAFS and QM/MM calculations. *Chem. Sci.* **2019**, *10*, 9807–9821.
- (21) Van Stappen, C.; Davydov, R.; Yang, Z.-Y.; Fan, R.; Guo, Y.; Bill, E.; Seefeldt, L. C.; Hoffman, B. M.; DeBeer, S. Spectroscopic Description of the E1 State of Mo Nitrogenase Based on Mo and Fe X-ray Absorption and Mössbauer Studies. *Inorg. Chem.* **2019**, *58*, 12365–12376.
- (22) Cao, L.; Caldararu, O.; Ryde, U. Protonation and Reduction of the FeMo Cluster in Nitrogenase Studied by Quantum Mechanics/Molecular Mechanics (QM/MM) Calculations. *J. Chem. Theory Comput.* **2018**, *14*, 6653–6678.
- (23) Varley, J. B.; Wang, Y.; Chan, K.; Studt, F.; Nørskov, J. K. Mechanistic insights into nitrogen fixation by nitrogenase enzymes. *Phys. Chem. Chem. Phys.* **2015**, *17*, 29541–29547.
- (24) Dance, I. Survey of the Geometric and Electronic Structures of the Key Hydrogenated Forms of FeMo-co, the Active Site of the Enzyme Nitrogenase: Principles of the Mechanistically Significant Coordination Chemistry. *Inorganics* **2019**, *7*, 8.
- (25) Pelmentschikov, V.; Case, D. A.; Noodleman, L. Ligand-Bound S=1/2 FeMo-Cofactor of Nitrogenase: Hyperfine Interaction Analysis and Implication for the Central Ligand X Identity. *Inorg. Chem.* **2008**, *47*, 6162–6172.
- (26) Fisher, K.; Dilworth, M. J.; Kim, C.-H.; Newton, W. E. *Azotobacter vinelandii* Nitrogenases Containing Altered MoFe Proteins with Substitutions in the FeMo-Cofactor Environment: Effects on the Catalyzed Reduction of Acetylene and Ethylene. *Biochemistry* **2000**, *39*, 2970–2979.
- (27) Fisher, K.; Lowe, D. J.; Tavares, P.; Pereira, A. S.; Huynh, B. H.; Edmondson, D.; Newton, W. E. Conformations generated during turnover of the *Azotobacter vinelandii* nitrogenase MoFe protein and their relationship to physiological function. *J. Inorg. Biochem.* **2007**, *101*, 1649–1656.
- (28) Lukoyanov, D.; Barney, B. M.; Dean, D. R.; Seefeldt, L. C.; Hoffman, B. M. Connecting nitrogenase intermediates with the kinetic scheme for N<sub>2</sub> reduction by a relaxation protocol and identification of the N<sub>2</sub> binding state. *Proc. Natl. Acad. Sci.* **2007**, *104*, 1451–1455.
- (29) Lukoyanov, D. A.; Khadka, N.; Yang, Z.-Y.; Dean, D. R.; Seefeldt, L. C.; Hoffman, B. M. Hydride Conformers of the Nitrogenase FeMo-cofactor Two-Electron Reduced State E<sub>2</sub>(2H), Assigned Using Cryogenic Intra Electron Paramagnetic Resonance Cavity Photolysis. *Inorg. Chem.* **2018**, *57*, 6847–6852.
- (30) Thorhallsson, A. T.; Bjornsson, R. The E<sub>2</sub> state of FeMoco: Hydride Formation versus Fe Reduction and a Mechanism for H<sub>2</sub> Evolution. *Chem.—Eur. J.* **2021**, DOI: 10.1002/chem.202102730.
- (31) Davis, L. C.; Henzl, M. T.; Burris, R. H.; Orme-Johnson, W. H. Iron-sulfur clusters in the molybdenum-iron protein component of nitrogenase. Electron paramagnetic resonance of the carbon monoxide inhibited state. *Biochemistry* **1979**, *18*, 4860–4869.
- (32) Christie, P. D.; Lee, H.-I.; Cameron, L. M.; Hales, B. J.; Orme-Johnson, W. H.; Hoffman, B. M. Identification of the CO-Binding Cluster in Nitrogenase MoFe Protein by ENDOR of <sup>57</sup>Fe Isotopomers. *J. Am. Chem. Soc.* **1996**, *118*, 8707–8709.
- (33) Lee, H.-I.; Cameron, L. M.; Hales, B. J.; Hoffman, B. M. CO Binding to the FeMo Cofactor of CO-Inhibited Nitrogenase: <sup>13</sup>CO and <sup>1</sup>H Q-Band ENDOR Investigation. *J. Am. Chem. Soc.* **1997**, *119*, 10121–10126.
- (34) Maskos, Z.; Hales, B. J. Photo-lability of CO bound to Mo-nitrogenase from *Azotobacter vinelandii*. *J. Inorg. Biochem.* **2003**, *93*, 11–17.
- (35) Lee, H.-I.; Hales, B. J.; Hoffman, B. M. Metal-Ion Valencies of the FeMo Cofactor in CO-Inhibited and Resting State Nitrogenase by <sup>57</sup>Fe Q-Band ENDOR. *J. Am. Chem. Soc.* **1997**, *119*, 11395–11400.
- (36) Sørli, M.; Christiansen, J.; Lemon, B. J.; Peters, J. W.; Dean, D. R.; Hales, B. J. Mechanistic features and structure of the nitrogenase alpha-Gln195 MoFe protein. *Biochemistry* **2001**, *40*, 1540–1549.
- (37) Yan, L.; Pelmentschikov, V.; Dapper, C. H.; Scott, A. D.; Newton, W. E.; Cramer, S. P. IR-Monitored Photolysis of CO-Inhibited Nitrogenase: A Major EPR-Silent Species with Coupled Terminal CO Ligands. *Chem.—Eur. J.* **2012**, *18*, 16349–16357.
- (38) *Prokaryotic Nitrogen Fixation: A Model System for the Analysis of a Biological Process*, 1st ed.; Triplett, E. W., Ed.; Horizon Press: Wymondham, 2000.
- (39) George, S. J.; Ashby, G. A.; Wharton, C. W.; Thorneley, R. N. F. Time-Resolved Binding of Carbon Monoxide to Nitrogenase Monitored by Stopped-Flow Infrared Spectroscopy. *J. Am. Chem. Soc.* **1997**, *119*, 6450–6451.
- (40) Yang, Z. Y.; Seefeldt, L. C.; Dean, D. R.; Cramer, S. P.; George, S. J. Steric Control of the Hi-CO MoFe Nitrogenase Complex Revealed by Stopped-Flow Infrared Spectroscopy. *Angew. Chem.* **2011**, *123*, 286–289.
- (41) Tolland, J. D.; Thorneley, R. N. F. Stopped-Flow Fourier Transform Infrared Spectroscopy Allows Continuous Monitoring of Azide Reduction, Carbon Monoxide Inhibition, and ATP Hydrolysis by Nitrogenase. *Biochemistry* **2005**, *44*, 9520–9527.
- (42) Yan, L.; Dapper, C. H.; George, S. J.; Wang, H.; Mitra, D.; Dong, W.; Newton, W. E.; Cramer, S. P. Photolysis of Hi-CO Nitrogenase - Observation of a Plethora of Distinct CO Species Using Infrared Spectroscopy. *Eur. J. Inorg. Chem.* **2011**, *2011*, 2064–2074.
- (43) Ibrahim, S. K.; Gormal, C. A.; Smith, B. E.; Pickett, C. J.; Vincent, K.; Best, S. P. The isolated iron-molybdenum cofactor of nitrogenase binds carbon monoxide upon electrochemically accessing reduced states. *Chem. Commun.* **1999**, 1019–1020.
- (44) Pickett, C. J.; Vincent, K. A.; Ibrahim, S. K.; Gormal, C. A.; Smith, B. E.; Best, S. P. Electron-Transfer Chemistry of the Iron-Molybdenum Cofactor of Nitrogenase: Delocalized and Localized Reduced States of FeMoco which Allow Binding of Carbon Monoxide to Iron and Molybdenum. *Chem.—Eur. J.* **2003**, *9*, 76–87.
- (45) Pickett, C. J.; Vincent, K. A.; Ibrahim, S. K.; Gormal, C. A.; Smith, B. E.; Fairhurst, S. A.; Best, S. P. Synergic Binding of Carbon Monoxide and Cyanide to the FeMo Cofactor of Nitrogenase: Relic Chemistry of an Ancient Enzyme? *Chem.—Eur. J.* **2004**, *10*, 4770–4776.

- (46) Spatzal, T.; Perez, K. A.; Einsle, O.; Howard, J. B.; Rees, D. C. Ligand binding to the FeMo-cofactor: Structures of CO-bound and reactivated nitrogenase. *Science* **2014**, *345*, 1620–1623.
- (47) Buscagan, T. M.; Perez, K. A.; Maggiolo, A. O.; Rees, D. C.; Spatzal, T. Structural Characterization of Two CO Molecules Bound to the Nitrogenase Active Site. *Angew. Chem., Int. Ed.* **2021**, *60*, 5704–5707.
- (48) Rod, T. H.; Nørskov, J. K. Modeling the Nitrogenase FeMo Cofactor. *J. Am. Chem. Soc.* **2000**, *122*, 12751–12763.
- (49) Dance, I. Calculated vibrational frequencies for FeMo-co, the active site of nitrogenase, bearing hydrogen atoms and carbon monoxide. *Dalton Trans.* **2011**, *40*, 6480–6489.
- (50) Varley, J. B.; Nørskov, J. K. First-Principles Calculations of Fischer-Tropsch Processes Catalyzed by Nitrogenase Enzymes. *ChemCatChem* **2013**, *5*, 732–736.
- (51) Scott, A. D.; Pelmenschikov, V.; Guo, Y.; Yan, L.; Wang, H.; George, S. J.; Dapper, C. H.; Newton, W. E.; Yoda, Y.; Tanaka, Y.; Cramer, S. P. Structural Characterization of CO-Inhibited Mo-Nitrogenase by Combined Application of Nuclear Resonance Vibrational Spectroscopy, Extended X-ray Absorption Fine Structure, and Density Functional Theory: New Insights into the Effects of CO Binding and the Role of the Interstitial Atom. *J. Am. Chem. Soc.* **2014**, *136*, 15942–15954.
- (52) Bergmann, J.; Oksanen, E.; Ryde, U. Quantum-refinement studies of the bidentate ligand of V-nitrogenase and the protonation state of CO-inhibited Mo-nitrogenase. *J. Inorg. Biochem.* **2021**, *219*, 111426.
- (53) Maskos, Z.; Fisher, K.; Sørli, M.; Newton, W. E.; Hales, B. J. Variant MoFe proteins of *Azotobacter vinelandii*: effects of carbon monoxide on electron paramagnetic resonance spectra generated during enzyme turnover. *J. Biol. Inorg. Chem.* **2005**, *10*, 394–406.
- (54) Rohde, M.; Laun, K.; Zebger, L.; Stripp, S. T.; Einsle, O. Two ligand-binding sites in CO-reducing V nitrogenase reveal a general mechanistic principle. *Sci. Adv.* **2021**, *7*, No. eabg4474.
- (55) Neese, F. The ORCA program system. *Wiley Interdiscip. Rev.: Comput. Mol. Sci.* **2012**, *2*, 73–78.
- (56) Neese, F. Software update: the ORCA program system, version 4.0. *Wiley Interdiscip. Rev.: Comput. Mol. Sci.* **2018**, *8*, No. e1327.
- (57) Neese, F.; Wennmohs, F.; Becker, U.; Riplinger, C. The ORCA quantum chemistry program package. *J. Chem. Phys.* **2020**, *152*, 224108.
- (58) Tao, J.; Perdew, J. P.; Staroverov, V. N.; Scuseria, G. E. Climbing the Density Functional Ladder: Nonempirical Meta-Generalized Gradient Approximation Designed for Molecules and Solids. *Phys. Rev. Lett.* **2003**, *91*, 146401.
- (59) Staroverov, V. N.; Scuseria, G. E.; Tao, J.; Perdew, J. P. Comparative assessment of a new nonempirical density functional: Molecules and hydrogen-bonded complexes. *J. Chem. Phys.* **2003**, *119*, 12129–12137.
- (60) Szilagy, R. K.; Winslow, M. A. On the accuracy of density functional theory for iron-sulfur clusters. *J. Comput. Chem.* **2006**, *27*, 1385–1397.
- (61) Sandala, G. M.; Hopmann, K. H.; Ghosh, A.; Noodleman, L. Calibration of DFT Functionals for the Prediction of <sup>57</sup>Fe Mössbauer Spectral Parameters in Iron-Nitrosyl and Iron-Sulfur Complexes: Accurate Geometries Prove Essential. *J. Chem. Theory Comput.* **2011**, *7*, 3232–3247.
- (62) Harris, T. V.; Szilagy, R. K. Iron-sulfur bond covalency from electronic structure calculations for classical iron-sulfur clusters. *J. Comput. Chem.* **2014**, *35*, 540–552.
- (63) Thorhallsson, A. T.; Benediktsson, B.; Björnsson, R. A model for dinitrogen binding in the E4 state of nitrogenase. *Chem. Sci.* **2019**, *10*, 11110–11124.
- (64) Henthorn, J. T.; Arias, R. J.; Koroidov, S.; Kröll, T.; Sokaras, D.; Bergmann, U.; Rees, D. C.; DeBeer, S. Localized Electronic Structure of Nitrogenase FeMoco Revealed by Selenium K-Edge High Resolution X-ray Absorption Spectroscopy. *J. Am. Chem. Soc.* **2019**, *141*, 13676–13688.
- (65) Grimme, S.; Antony, J.; Ehrlich, S.; Krieg, H. A consistent and accurate ab initio parametrization of density functional dispersion correction (DFT-D) for the 94 elements H–Pu. *J. Chem. Phys.* **2010**, *132*, 154104.
- (66) Grimme, S.; Ehrlich, S.; Goerigk, L. Effect of the damping function in dispersion corrected density functional theory. *J. Comput. Chem.* **2011**, *32*, 1456–1465.
- (67) Lenthe, E. v.; Baerends, E. J.; Snijders, J. G. Relativistic regular two-component Hamiltonians. *J. Chem. Phys.* **1993**, *99*, 4597–4610.
- (68) van Wüllen, C. Molecular density functional calculations in the regular relativistic approximation: Method, application to coinage metal diatomics, hydrides, fluorides and chlorides, and comparison with first-order relativistic calculations. *J. Chem. Phys.* **1998**, *109*, 392–399.
- (69) Weigend, F.; Ahlrichs, R. Balanced basis sets of split valence, triple zeta valence and quadruple zeta valence quality for H to Rn: Design and assessment of accuracy. *Phys. Chem. Chem. Phys.* **2005**, *7*, 3297–3305.
- (70) Pantazis, D. A.; Chen, X.-Y.; Landis, C. R.; Neese, F. All-Electron Scalar Relativistic Basis Sets for Third-Row Transition Metal Atoms. *J. Chem. Theory Comput.* **2008**, *4*, 908–919.
- (71) Neese, F. An improvement of the resolution of the identity approximation for the formation of the Coulomb matrix. *J. Comput. Chem.* **2003**, *24*, 1740–1747.
- (72) Neese, F.; Wennmohs, F.; Hansen, A.; Becker, U. Efficient, approximate and parallel Hartree-Fock and hybrid DFT calculations. A “chain-of-spheres” algorithm for the Hartree-Fock exchange. *Chem. Phys.* **2009**, *356*, 98–109.
- (73) Best, R. B.; Zhu, X.; Shim, J.; Lopes, P. E. M.; Mittal, J.; Feig, M.; MacKerell, A. D. Optimization of the Additive CHARMM All-Atom Protein Force Field Targeting Improved Sampling of the Backbone  $\phi$ ,  $\psi$  and Side-Chain  $\chi_1$  and  $\chi_2$  Dihedral Angles. *J. Chem. Theory Comput.* **2012**, *8*, 3257–3273.
- (74) Metz, S.; Kästner, J.; Sokol, A. A.; Keal, T. W.; Sherwood, P. C. hem S hell a modular software package for QM / MM simulations. *Wiley Interdiscip. Rev.: Comput. Mol. Sci.* **2014**, *4*, 101–110.
- (75) Sherwood, P.; et al. QUASI: A general purpose implementation of the QM/MM approach and its application to problems in catalysis. *J. Mol. Struct.: THEOCHEM* **2003**, *632*, 1–28.
- (76) Lovell, T.; Li, J.; Liu, T.; Case, D. A.; Noodleman, L. FeMo Cofactor of Nitrogenase: A Density Functional Study of States MN, MOX, MR, and MI. *J. Am. Chem. Soc.* **2001**, *123*, 12392–12410.
- (77) Cao, L.; Ryde, U. Influence of the protein and DFT method on the broken-symmetry and spin states in nitrogenase. *Int. J. Quantum Chem.* **2018**, *118*, No. e25627.
- (78) Raugei, S.; Seefeldt, L. C.; Hoffman, B. M. Critical computational analysis illuminates the reductive-elimination mechanism that activates nitrogenase for N<sub>2</sub> reduction. *Proc. Natl. Acad. Sci.* **2018**, *115*, E10521–E10530.
- (79) Grunenberg, J. The Interstitial Carbon of the Nitrogenase FeMo Cofactor is Far Better Stabilized than Previously Assumed. *Angew. Chem., Int. Ed.* **2017**, *56*, 7288–7291.
- (80) Cao, L.; Ryde, U. What Is the Structure of the E4 Intermediate in Nitrogenase? *J. Chem. Theory Comput.* **2020**, *16*, 1936–1952.
- (81) Barone, V.; Cossi, M. Quantum Calculation of Molecular Energies and Energy Gradients in Solution by a Conductor Solvent Model. *J. Phys. Chem. A* **1998**, *102*, 1995–2001.
- (82) York, D. M.; Karplus, M. A Smooth Solvation Potential Based on the Conductor-Like Screening Model. *J. Phys. Chem. A* **1999**, *103*, 11060–11079.
- (83) Mina-Camilde, N.; Manzanares, I. C.; Caballero, J. F. Molecular Constants of Carbon Monoxide at  $v = 0, 1, 2$ , and  $3$ : A Vibrational Spectroscopy Experiment in Physical Chemistry. *J. Chem. Educ.* **1996**, *73*, 804.
- (84) Björnsson, R.; Lima, F. A.; Spatzal, T.; Weyhermüller, T.; Glatzel, P.; Bill, E.; Einsle, O.; Neese, F.; DeBeer, S. Identification of a spin-coupled Mo(III) in the nitrogenase iron-molybdenum cofactor. *Chem. Sci.* **2014**, *5*, 3096–3103.

- (85) Chilkuri, V. G.; DeBeer, S.; Neese, F. Ligand Field Theory and Angular Overlap Model Based Analysis of the Electronic Structure of Homovalent Iron-Sulfur Dimers. *Inorg. Chem.* **2020**, *59*, 984–995.
- (86) Spiller, N.; Chilkuri, V. G.; DeBeer, S.; Neese, F. Sulfur vs. Selenium as Bridging Ligand in Di-Iron Complexes: A Theoretical Analysis. *Eur. J. Inorg. Chem.* **2020**, *2020*, 1525–1538.
- (87) Foster, J. M.; Boys, S. F. Canonical Configurational Interaction Procedure. *Rev. Mod. Phys.* **1960**, *32*, 300–302.
- (88) Hirshfeld, F. L. Bonded-atom fragments for describing molecular charge densities. *Theor. Chim. Acta* **1977**, *44*, 129–138.
- (89) Lu, T.; Chen, F. Multiwfn: A multifunctional wavefunction analyzer. *J. Comput. Chem.* **2012**, *33*, 580–592.
- (90) Bultinck, P.; Van Alsenoy, C.; Ayers, P. W.; Carbó-Dorca, R. Critical analysis and extension of the Hirshfeld atoms in molecules. *J. Chem. Phys.* **2007**, *126*, 144111.
- (91) Melo, M. C. R.; Bernardi, R. C.; Rudack, T.; Scheurer, M.; Riplinger, C.; Phillips, J. C.; Maia, J. D. C.; Rocha, G. B.; Ribeiro, J. V.; Stone, J. E.; Neese, F.; Schulten, K.; Luthey-Schulten, Z. NAMD goes quantum: an integrative suite for hybrid simulations. *Nat. Methods* **2018**, *15*, 351–354.
- (92) Gade, L. H. *Koordinationschemie*, 1st ed.; Wiley: Weinheim, 2010.
- (93) King, R. B.; Bitterwolf, T. E. Metal carbonyl analogues of iron-sulfur clusters found in metalloenzyme chemistry. *Coord. Chem. Rev.* **2000**, *206–207*, 563–579.
- (94) Beinert, H.; Holm, R. H.; Münck, E. Iron-Sulfur Clusters: Nature's Modular, Multipurpose Structures. *Science* **1997**, *277*, 653–659.
- (95) Harris, T. V.; Szilagy, R. K. Comparative Assessment of the Composition and Charge State of Nitrogenase FeMo-Cofactor. *Inorg. Chem.* **2011**, *50*, 4811–4824.
- (96) Rees, J. A.; Bjornsson, R.; Kowalska, J. K.; Lima, F. A.; Schlesier, J.; Sippel, D.; Weyhermüller, T.; Einsle, O.; Kovacs, J. A.; DeBeer, S. Comparative electronic structures of nitrogenase FeMoco and FeVco. *Dalton Trans.* **2017**, *46*, 2445–2455.
- (97) Spatzal, T.; Perez, K. A.; Howard, J. B.; Rees, D. C. Catalysis-dependent selenium incorporation and migration in the nitrogenase active site iron-molybdenum cofactor. *eLife* **2015**, *4*, No. e11620.
- (98) Sharma, S.; Sivalingam, K.; Neese, F.; Chan, G. K.-L. Low-energy spectrum of iron-sulfur clusters directly from many-particle quantum mechanics. *Nat. Chem.* **2014**, *6*, 927–933.
- (99) Li, Z.; Guo, S.; Sun, Q.; Chan, G. K.-L. Electronic landscape of the P-cluster of nitrogenase as revealed through many-electron quantum wavefunction simulations. *Nat. Chem.* **2019**, *11*, 1026–1033.
- (100) Li, Z.; Li, J.; Dattani, N. S.; Umrigar, C. J.; Chan, G. K.-L. The electronic complexity of the ground-state of the FeMo cofactor of nitrogenase as relevant to quantum simulations. *J. Chem. Phys.* **2019**, *150*, 024302.
- (101) Benediktsson, B.; Bjornsson, R. Quantum Mechanics/Molecular Mechanics Study of Resting-State Vanadium Nitrogenase: Molecular and Electronic Structure of the Iron-Vanadium Cofactor. *Inorg. Chem.* **2020**, *59*, 11514–11527.
- (102) Yang, Z.-Y.; Jimenez-Vicente, E.; Kallas, H.; Lukoyanov, D. A.; Yang, H.; Martin del Campo, J. S.; Dean, D. R.; Hoffman, B. M.; Seefeldt, L. C. The electronic structure of FeV-cofactor in vanadium-dependent nitrogenase. *Chem. Sci.* **2021**, *12*, 6913–6922.
- (103) Rohde, M.; Grunau, K.; Einsle, O. CO Binding to the FeV Cofactor of CO-Reducing Vanadium Nitrogenase at Atomic Resolution. *Angew. Chem., Int. Ed.* **2020**, *59*, 23626.
- (104) Watson, L.; Eisenstein, O. Entropy Explained: The Origin of Some Simple Trends. *J. Chem. Educ.* **2002**, *79*, 1269.
- (105) Kästner, J.; Blöchl, P. E. Model for Acetylene Reduction by Nitrogenase Derived from Density Functional Theory. *Inorg. Chem.* **2005**, *44*, 4568–4575.
- (106) Hallmen, P. P.; Kästner, J. N<sub>2</sub> Binding to the FeMo-Cofactor of Nitrogenase. *Z. Anorg. Allg. Chem.* **2015**, *641*, 118–122.
- (107) Dance, I. How feasible is the reversible S-dissociation mechanism for the activation of FeMo-co, the catalytic site of nitrogenase? *Dalton Trans.* **2019**, *48*, 1251–1262.
- (108) Skubi, K. L.; Holland, P. L. So Close, yet Sulfur Away: Opening the Nitrogenase Cofactor Structure Creates a Binding Site. *Biochemistry* **2018**, *57*, 3540–3541.
- (109) Seefeldt, L. C.; Yang, Z.-Y.; Lukoyanov, D. A.; Harris, D. F.; Dean, D. R.; Rauegi, S.; Hoffman, B. M. Reduction of Substrates by Nitrogenases. *Chem. Rev.* **2020**, *120*, 5082–5106.
- (110) Einsle, O.; Rees, D. C. Structural Enzymology of Nitrogenase Enzymes. *Chem. Rev.* **2020**, *120*, 4969–5004.
- (111) Jasnowski, A. J.; Lee, C. C.; Ribbe, M. W.; Hu, Y. Reactivity, Mechanism, and Assembly of the Alternative Nitrogenases. *Chem. Rev.* **2020**, *120*, 5107–5157.